Freezing conditions in warm disks: snowlines and their effect on the chemical structure of planet-forming disks

Leemker, M.

Chapter 6

Chemistry across dust and gas gaps in protoplanetary disks: modelling the co-spatial molecular rings in the HD 100546 disk

M. Leemker, A. S. Booth, E. F. van Dishoeck, L. Wölfer, B. Dent

In preparation

Abstract

Context. Large and nearby protoplanetary disks are commonly marked by prominent rings in the continuum emission, possibly carved by forming planets. High-resolution ALMA observations show that both the dust and the gas is structured. These molecular structures in the gas can be due to physical rings in the gas and dust density structure and/ or chemical rings. The aim of this work is to identify the expected location and intensity of rings seen in molecular line emission in gapped disks for a range of physical conditions across the gap. The molecular ring locations are compared to the location of the dust rings. In particular, we aim to model the molecular rings that are co-spatial with the dust in the HD 100546 disk using the thermochemical code DALI.
Aims. We analyze ALMA observations of CO isotopologues, [C I], HCN, CN, C_2H, NO, and HCO^+ in the HD 100546 disk. A thermochemical model reproducing the CO isotopologue observations and the double ring seen in continuum emission is used to make predictions for various emission lines. The effect of the amount of gas in the dust gap, the C/O ratio, an attenuated background UV radiation field, and the flaring index of the disk on the distributions are investigated.
Results. The fiducial model of a gapped disk that provides a good fit to the continuum and the CO isotopologues, does not reproduce the morphology or the intensity of the [C I], CN, C_2H, and NO observations. The HCN and HCO^+ intensities on the other hand, are reproduced within a factor of a few in most disk regions. The CO and HCO^+ column densities are directly related to the gas gap depth and the CO isotopologue emission is consistent with a shallow gas gap of a factor of ten less gas. In contrast, a much deeper gap of at least four orders of magnitude less gas is needed to create a ring in the CN, C_2H, and NO column densities due to the increasing stellar UV field in the gap. The interstellar UV field creates an outer ring in C_2H and NO at $\sim 250-400$ au. Additionally, models predict that the HCN, CN, C_2H, NO, and HCO^+ are abundant at a high disk layer of $z/r = 0.2 - 0.35$, in contrast to the observations in the same disk indicating $z/r \leq 0.1$. The models underpredict the [C I] and C_2H emission by a factor of at least ten and 50, respectively, in most disk regions, whereas the CN intensity is reproduced within a factor of a few. Increasing the C/O ratio from 0.99 to 1.01 increases the column density and intensity of CN, and C_2H by one and two orders of magnitude, respectively, whereas that of C increases by less than a factor of two.
Conclusions. The molecular rings predicted by thermochemical models do not naturally coincide with those seen in the dust. The rings seen in the HD 100546 disk can be best produced with a gas gap deeper than expected from the CO isotopologue emission, a C/O ratio of ~ 1, and an attenuated background UV field.

6.1 Introduction

The gas, dust, and ice surrounding a young star are the building blocks of new planets. Many of the bright and large protoplanetary disks have been observed to not be smooth but have gaps, rings, and arcs in the continuum that are possibly carved by massive forming planets (e.g., Andrews et al. 2018; Huang et al. 2018; Long et al. 2018; Andrews 2020; Francis & van der Marel 2020). Recently, young planets with clear accretion signatures have been directly detected in the PDS 70 disk (Keppler et al. 2018; Haffert et al. 2019; Benisty et al. 2021), point-like sources possibly due to young planets are seen in the HD 169142 disk (Hammond et al. 2023)) and are debated in the AB Aur disk Currie et al. 2022; Zhou et al. 2023), and promising signs of planets through indirect methods such as CO gas kinematics are seen in many other disks (e.g., Pinte et al. 2018b; Teague et al. 2018a; Pinte et al. 2019; Izquierdo et al. 2022, 2023). The chemical composition of the solid core and gaseous atmosphere of these planets depends on the chemical composition of the ice on the dust grains and the gas in their protoplanetary disk. Comparing the composition in a protoplanetary disk to that measured in exoplanet atmospheres provides insights into where and when these planets have formed (Öberg et al. 2011; Öberg & Bergin 2016; Cridland et al. 2016; Mordasini et al. 2016; Cridland et al. 2017, 2023; Eistrup 2023).

The chemical composition of the gas and ice across a disk is not constant. Signs of chemical substructures have been found in simple gas-phase molecules such as the commonly observed HCO^+, N_2H^+, CN, HCN, and the recently detected NO (e.g., Cazzoletti et al. 2018; Bergner et al. 2019; Qi et al. 2019; Aikawa et al. 2021; Bergner et al. 2021; Law et al. 2021a; Zhang et al. 2021; Leemker et al. 2023; Temmink et al. 2023). These structures are seen both at the location of dust structures such as rings, gaps, and arcs, as well as in smooth regions of the disk. These ringed structures can thus be due to chemical rings, locally enhancing the abundance of a chemical species, or a physical ring in the underlying gas density structure.

Young planets that are embedded in their native protoplanetary disk can carve a deep gap in the dust, and if they are sufficiently massive, also a gap in the gas as traced by CO emission (Bruderer et al. 2014; Zhu et al. 2014; Dong et al. 2015b; Rosotti et al. 2016; Andrews et al. 2018; Long et al. 2018; Binkert et al. 2021; Öberg et al. 2021). These gaps and cavities seen in CO gas are typically shallower than those in the dust (e.g., van der Marel et al. 2016; Fedele et al. 2017; Zhang et al. 2021; Leemker et al. 2022). Moreover, some disks with gaps seen in the dust do not show a gap in the CO gas at the same location, for example the IM Lup and GM Aur disks outside 50 au (Zhang et al. 2021). A gas gap in a planet forming disk not only reduces the amount of gas and dust at that location, it also increases the intensity of the UV radiation as there is less dust to shield the UV (Cleeves et al. 2011; Facchini et al. 2018; Alarcón et al. 2020; Rab et al. 2020). This in turn leads to an increase of the dust temperature. The resulting gas temperature in the dust gap is a balance of the heating and cooling processes and can be either warmer or colder than the region just outside the gap. This change in temperature and UV field across the gap could lead to rings in other molecules as the chemistry

in disks is sensitive to both of these.

With the increasing number of high-resolution ALMA observations resolving the gaps and cavities not only in the dust, but also in the gas across multiple disks we can now test predictions of the models (e.g., Öberg et al. 2021). Modelling of CO, the most abundant molecule in disks after H_2, across gaps and cavities has shown that it remains abundant down to very low gas column densities where photodissociation becomes important (Woitke et al. 2009; Bruderer 2013). As the abundance of CO and its isotopologues does not change drastically across the gap, the optically thin isotopologues can be used to measure the depth of the gap whereas the optically thick ones can be used to measure the temperature (e.g., Fedele et al. 2017; Facchini et al. 2018; Alarcón et al. 2020; Calahan et al. 2021; Leemker et al. 2022). Additionally, modelling of HCO^+ isotopologues across a gap shows that the ratio of DCO^+ to HCO^+ or $H^{13}CO^+$ is sensitive to the amount of gas in the gap (Smirnov-Pinchukov et al. 2020).

Chemical rings can be caused by snowlines of the major volatiles: H_2O, NH_3, CO_2, CO, and N_2. These snowlines are the midplane locations where 50% of a molecule is in the gas-phase and 50% is frozen out onto the dust grains. This is exceptionally clear in the structure of HCO^+ and N_2H^+. These molecules respond very strongly to the desorption of H_2O, CO, and N_2, resulting in ring-shaped emission outside, at, or inside the snowline (Qi et al. 2013; van 't Hoff et al. 2017; Leemker et al. 2021). On top of that, the abundance of HCO^+, DCO^+, and N_2H^+ is set by the ionisation rate in the disk which may radially change due to substructures (e.g., Aikawa & Herbst 2001; Cleeves et al. 2014a; Aikawa et al. 2021).

In addition to snowlines, the stellar UV field is important for setting the chemistry in disks by photodissociating molecules in the surface layers of the disk. This not only destroys molecules, but it also enables formation paths to new ones. For example, the photodissociation of water can lead to the formation of NO and the photodissociation of CO leads to the presence of atomic carbon in disks (Thi et al. 2010; Bruderer et al. 2012; Schwarz & Bergin 2014; Leemker et al. 2023). Moreover, UV radiation can vibrationally excite molecular hydrogen (H_2^*) at intermediate disk radii. The extra energy stored in H_2^* can then be used to overcome the energy barrier to form CN and NO. Both models and observations show that CN is present in the surface layers of disks which is consistent with CN tracing the UV in the disk atmosphere (Visser et al. 2018; Cazzoletti et al. 2018; Paneque-Carreño et al. 2022). Apart from the innermost regions in the midplane, HCN follows the same trend as it is closely related to CN in the disk surface layers. Therefore, ring-shaped CN and HCN emission is expected even if the underlying gas and dust surface density profiles are smooth (Long et al. 2021).

In summary, molecular emission is not necessarily expected to follow the underlying physical structure of the disk such as rings, gaps, and cavities. This is clearly found in the observations of the five disks of the MAPS (Molecules with ALMA at Planet-forming Scales) program, where the structures seen in molecular line emission do not correlate with those in the dust apart from the MWC 480 disk and the inner 150 au (Law et al. 2021a; Jiang et al. 2022). Three other disks are a notable exception to this: the PDS 70, IRS 48, and the HD 100546 disks, where

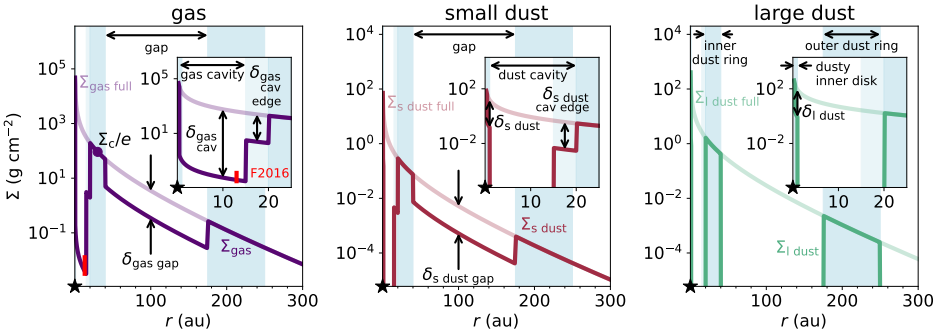

Figure 6.1: Surface density of the gas (purple), small dust (red), and large dust (green) in the fiducial model for the HD 100546 disk. The light purple, red, and green lines indicate the respective surface densities in a full disk without any gaps, cavities and rings. The blue shaded regions indicate the dusty inner disk and the two dust rings at 20-40 au and 175-250 au respectively. The surface density Σ_c/e at r_c is indicated with a scatter point in the left panel. Additionally, the DALI parameters that control drops and increases in the surface densities are indicated with arrows (see Table 6.B.1 for their values). The red bar in the inset in the left panel indicates the gas surface density based on CO by Fedele et al. (2016). The small insets in each panel focus on the inner 25 au of the disk.

small molecules such as HCO^+, C_2H, NO, CS, SO, or SO_2 and complex organic molecules such as CH_3OH or CH_3OCH_3 are detected (Facchini et al. 2021; van der Marel et al. 2021b; Booth et al. 2021b,c; Brunken et al. 2022; Leemker et al. 2023; Booth et al. 2023a). These disks are all transition disks with a large cavity seen in the dust and in case of e.g., the PDS 70 IRS 48, HD 169142, and HD 135344B disks also in the gas also in the gas. For the PDS 70 and IRS 48 disks, the molecular line emission is seen at the dust ring/ trap that is just outside a deep cavity in both the gas and dust, which could reduce the molecular line emission due to a lack of gas inside the cavities. In contrast, besides from a small central cavity ($r \lesssim 15$ au), the HD 100546 disk does not show signs of a deep gap in the gas in the outer disk, yet the molecular rings are found to be coincident with the dust rings (Walsh et al. 2014a; Pinilla et al. 2015; Fedele et al. 2021, Booth et al. in prep.).

In this paper we aim to investigate the conditions that lead to molecular rings coinciding with the dust rings. In Sect. 6.2 we present the [C I] data in the HD 100546 disk and describe the setup of our thermochemical models that include a gas and dust cavity as well as a gap between the two rings seen in the HD 100546 continuum and CO isotopologues. In addition, we present a fiducial model that fits these data. Section 6.3 presents the predictions for [C I], HCN, CN, C_2H, NO, and HCO^+ in this disk under different physical conditions, varying parameters such as a deep gas gap, an elevated C/O ratio, an attenuated background UV field, and disk flaring. The results are discussed in Sect. 6.4 in the specific context of the HD 100546 observations and our conclusions are summarized in Sect. 6.5.

6.2 Methods

6.2.1 Source: HD 100546

HD 100546 is a ~ 2 $M_\odot$, 5 Myr old Herbig Ae/Be star with a luminosity of $\sim$36 $L_\odot$ (Kama et al. 2016; Arun et al. 2019; Pineda et al. 2019). This star is located in a relatively isolated region at a distance of 108.1 ± 0.4 pc (Gaia Collaboration et al. 2016, 2023). The star is surrounded by a massive and gas-rich disk of $0.03-0.1$ $M_\odot$ based on CO isotopologue emission and an upper limit on the HD flux (Kama et al. 2016; Stapper et al. 2023). Both the CO gas and the dust in this disk are highly structured with small scale gas and dust spirals (a few $0\farcs1$), a large scale ($\sim$ 1") dusty spiral and a large scale spiral in the gas kinematics (Garufi et al. 2016; Follette et al. 2017; Sissa et al. 2018; Norfolk et al. 2022; Wölfer et al. 2023a). Additionally, the continuum emission in this disk is seen in three locations: an unresolved dusty inner disk, a bright inner ring from $\sim$ 20 au to 40 au, and a weak outer ring at $< 1\%$ of the peak continuum intensity from $\sim$ 150 au to 250 au (Bruderer et al. 2012; Walsh et al. 2014a; Pineda et al. 2019; Fedele et al. 2021).

The central cavity and gap between the two dust rings have been hypothesized to be carved by massive planets. The inner planet has been inferred from CO rovibrational emission and a feature seen in scattered light (e.g., Brittain et al. 2013, 2014; Currie et al. 2015). In addition, co-rotating SO is seen at the location of the proposed planet (Booth et al. 2023b). A second planet has been hypothesized between the two dust rings as a point source is seen at $50 - 60$ au in scattered light observations (Quanz et al. 2013a; Currie et al. 2014). However, the nature of these potential planets is debated as no accretion signatures have been found at this location and different results have been found depending on the data quality and imaging techniques (Currie et al. 2017; Follette et al. 2017; Rameau et al. 2017). Therefore, more research is needed to firmly conclude if these planets are present.

ALMA observations of molecular lines have revealed a number of different molecules in this disk. The detection of formaldehyde and the complex organic molecule methanol in this warm disk indicates that the molecular inventory is likely inherited from the native dark cloud as the bulk of the disk is too warm for CO freeze-out (Booth et al. 2021c). The CS and SO emission are somewhat asymmetric to opposite sites of the disk, hinting at an overdensity of material close to the star shadowing the outer disk and causing an azimuthally varying C/O ratio (Keyte et al. 2023). Finally, many of the molecular lines except the CO isotopologues are close to co-spatial with the rings seen in the dust (Booth et al. 2023a, see also Fig. 6.5). In this work, we use high resolution ALMA observations of the dust and CO isotopologues (Pineda et al. 2019; Pérez et al. 2020; Wölfer et al. 2023b,a), intermediate resolution data of the dust, CO, $C^{17}O$, HCN, CN, C_2H, NO, and HCO^+ (Booth et al. 2023a), and [C I] observations.

6.2.2 ALMA data covering [C I]

The ^{12}CO $J = 7 - 6$ and [C I] line emission data used in his paper were taken in Cycle 6 with ALMA in Band 10 (2018.1.00141.S; PI: B. Dent), using 43 antennas with baselines of 15-783 m. Starting from the archival pipeline-calibrated data we performed further data reduction using CASA (McMullin et al. 2007). Due to a low signal-to-noise ratio, no self-calibration was applied. We first subtracted the continuum using the `uvcontsub` task, flagging channels containing line emission, and then imaged the lines with `tCLEAN` for both the continuum-subtracted and non-subtracted data sets. In this process, we imaged the data at the highest spectral resolution possible and adopted a Briggs robust weighting of 0.5, which gave the best trade off between spatial resolution and sensitivity. We also applied a Keplerian mask [1] using an inclination of 42 °, position angle of 320 °, distance of 110 pc, stellar mass of 2.13 $M_\odot$, and systemic velocity of 5.7 km s^{-1}. We further used the multi-scale deconvolver (scales 0,5,10,20) and a slight `uv-taper` ($0\farcs05 \times 0\farcs05, 0\,°$) to improve the signal-to-noise ratio in the images. The integrated intensity map and the spectrum are presented in Fig. 6.A.1.

6.2.3 DALI

To investigate the relative importance of physical versus chemical rings, we model the dust rings and rings seen in molecular line emission using the thermochemical code Dust And LInes (DALI; Bruderer et al. 2009, 2012; Bruderer 2013). The model presented in this work is based on those presented in Pirovano et al. (2022) and Keyte et al. (2023). We improve on the dust structure from the latter model by including a dust gap in the outer disk to match the double ringed structure of the continuum observations (Fedele et al. 2021; Booth et al. 2023a). Additionally, the gas density structure is improved by including a gas gap between the two dust rings and by including an inner gas cavity just inside the inner dust ring at 20 au to match the observed CO emission in those regions (Pérez et al. 2020; Booth et al. 2023a; Wölfer et al. 2023a). The general setup of the model is described below.

6.2.3.1 Gas density structure

The radial and vertical density structure of the disk follow the standard DALI setup for a flared disk with an exponentially tapered power law in the radial direction and a Gaussian distribution of the gas in the vertical direction (see Bruderer 2013, and Appendix 6.B.1.1 for details). To include the gas cavity and a gas gap in this disk, the gas surface density of the full disk is lowered as follows:

$$\Sigma_{\rm gas} = \begin{cases} \Sigma_{\rm gas\ full} \times 10^{-5} & (0.4\ {\rm au} < r < 15\ {\rm au}) \\ \Sigma_{\rm gas\ full} \times 10^{-2} & (15\ {\rm au} < r < 20\ {\rm au}) \\ \Sigma_{\rm gas\ full} & (20\ {\rm au} < r < 40\ {\rm au}) \\ \Sigma_{\rm gas\ full} \times \delta_{\rm gas\ gap} & (40\ {\rm au} < r < 175\ {\rm au}) \\ \Sigma_{\rm gas\ full} & (175\ {\rm au} < r < 1000\ {\rm au}), \end{cases} \tag{6.1}$$

[1] `https://github.com/richteague/keplerian_mask`

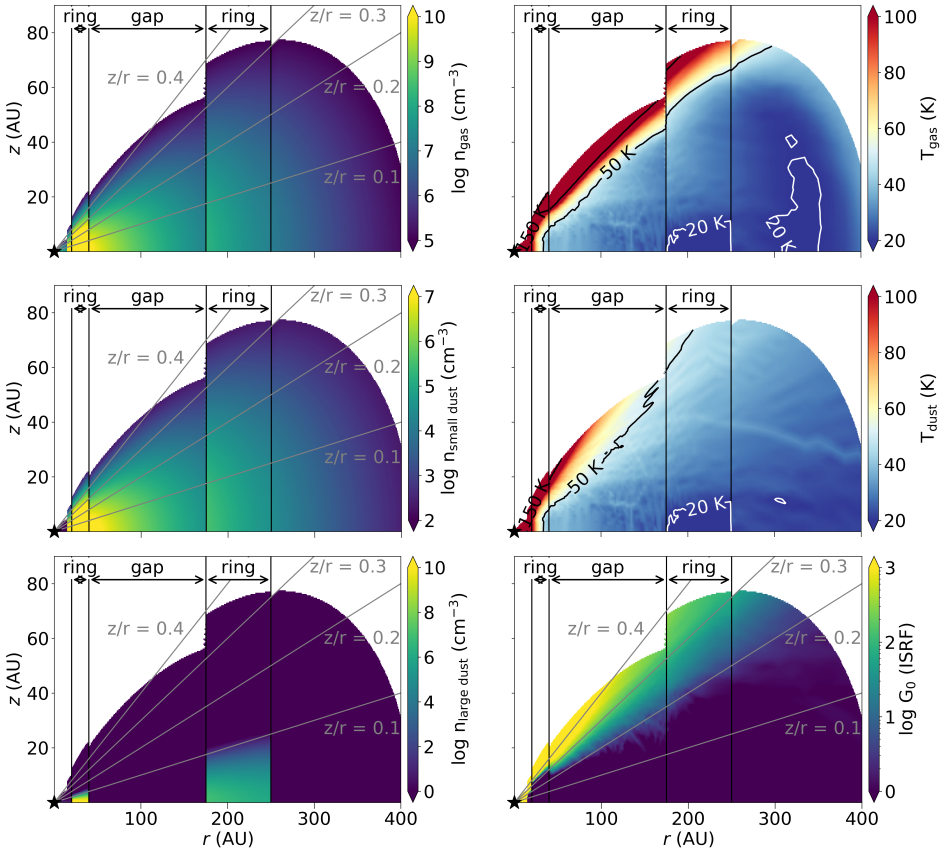

Figure 6.2: Structure of the fiducial DALI model. From left to right and top to bottom: gas, small dust, and large dust density, gas and dust temperature, and UV field. Only the regions with a gas number density above 10^5 cm^{-3} are shown. Outside 250 au, the midplane gas density is too low for the gas and dust temperature to be coupled.

with $\delta_{\rm gas\ gap}$ lowering the gas density in the gap, see the left panel of Fig. 6.1 and the top left panel of Fig. 6.2.

6.2.3.2 Dust density structure

The small grains follow the gas outside the inner gas cavity as they are expected to be well mixed with the gas. Outside the gas cavity but inside the dust cavity the small grains also follow the gas. Inside the gas cavity down to the dusty inner disk that is observed in continuum emission up to $<$ 2 au (Benisty et al. 2010; Pineda et al. 2019; Pérez et al. 2020), the small grains are depleted by a factor of 10^{-10} to mimic a cavity devoid of any dust. The dusty inner disk inside 1 au is depleted in small (5 nm$-$1 μm) and large (5 nm$-$1 mm) grains by a factor of 10^{-2} (see also the middle and right panels in Fig. 6.1 and the middle left and bottom

left panels Fig. 6.2):

$$\Sigma_{\text{s dust}} = \begin{cases} \Sigma_{\text{s dust full}} \times 10^{-2} & (0.4 \text{ au} < r < 1 \text{ au}) \\ \Sigma_{\text{s dust full}} \times 10^{-10} & (1 \text{ au} < r < 15 \text{ au}) \\ (1 - f_{\text{ls}}) \times \Sigma_{\text{gas}}/\Delta_{\text{gd}} & (15 \text{ au} < r < 1000 \text{ au}). \end{cases} \tag{6.2}$$

In the vertical direction the small dust follows the gas.

Observations show that the large dust in the HD 100546 disk is mainly present at three different locations: a dusty inner disk, an inner ring at $20 - 40$ au and an outer ring at $175 - 250$ au (Walsh et al. 2014a; Pineda et al. 2019; Fedele et al. 2021). The cavity in the large dust in our model is 5 au larger than that in the small dust and the gas, similar to what is observed in other transition disks (Perez et al. 2015; van der Marel et al. 2016; Leemker et al. 2022; Wölfer et al. 2023b). This is parametrized as:

$$\Sigma_{\text{l dust}} = \begin{cases} \Sigma_{\text{l dust full}} \times 10^{-2} & (0.4 \text{ au} < r < 1 \text{ au}) \\ \Sigma_{\text{l dust full}} \times 10^{-10} & (1 \text{ au} < r < 20 \text{ au}) \\ \Sigma_{\text{l dust full}} & (20 \text{ au} < r < 40 \text{ au}) \\ \Sigma_{\text{l dust full}} \times 10^{-10} & (40 \text{ au} < r < 175 \text{ au}) \\ \Sigma_{\text{l dust full}} & (175 \text{ au} < r < 250 \text{ au}) \\ \Sigma_{\text{l dust full}} \times 10^{-10} & (250 \text{ au} < r < 1000 \text{ au}). \end{cases} \tag{6.3}$$

The outer ring extends to 250 au, see also the right panel of Fig. 6.1. Additionally, the large grains are settled to the disk midplane (bottom left panel in Fig. 6.2). The dust in the midplane of the outer dust ring is sufficiently cold for some CO freeze-out as the dust temperature drops below 20 K (middle row, right panel in Fig. 6.2).

6.2.4 Stellar spectrum

The stellar spectrum of HD 100546 observed by the Far Ultraviolet Spectroscopic Explorer (FUSE) and the the International Ultraviolet Explorer (IUE) and presented in Bruderer et al. (2012) is used. These observations have been dereddend and extended to longer wavelengths using a B9V template (Pickles 1998). Additionally, an X-ray luminosity of 7.9×10^{28} erg s^{-1} (Stelzer et al. 2006) with a temperature of 7×10^7 K is included to account for more energetic radiation.

6.2.5 Chemistry

The chemistry is modelled using a chemical network suited for modelling small nitrogen bearing molecules such as CN, HCN, and NO, and small hydrocarbons such as C_2H. This network was first presented in Visser et al. (2018); Cazzoletti et al. (2018); and Long et al. (2021). Similar to Leemker et al. (2023), the binding energy of C_2H_3 (ethylenyl) is set to 10^4 K to mimic the conversion of C_2H_3 to larger COMs on the grain surfaces. This network includes the main gas-phase formation and destruction routes of the molecules of interest, the freeze-out and thermal-,

and non-desorption of the major volatiles. The non-thermal desorption rates of H_2O and CO are updated from 1.3×10^{-3} and 2.7×10^{-3} molecules desorbed per grain per incident UV photon to 5×10^{-4} and 1.4×10^{-3} molecules desorbed per grain per incident UV photon respectively (Öberg et al. 2007, 2009; Paardekooper et al. 2016; González Díaz et al. 2019; Fillion et al. 2022). Additionally, some grain surface reactions are included such as the formation of H_2 on grains and PAHs. Moreover, the hydrogenation of O, C, N, and CN on grains to form H_2O, CH_4, NH_3, and HCN ices are included, but no detailed ice chemistry such as the conversion of CO to H_2CO or CH_3OH is modelled as the HD 10546 disk is warm and no large-scale CO freeze-out is expected.

The abundance of the CO isotopologues is predicted with the CO isotopologue network presented in Miotello et al. (2016). This network includes the ^{12}C, ^{13}C, ^{16}O, ^{17}O, and ^{18}O isotopes, with their ratios taken as $^{12}C/^{13}C = 77$, $^{16}O/^{18}O = 560$, and $^{16}O/^{17}O = 1792$ (Wilson & Rood 1994). Both chemical networks are started with molecular initial conditions and a fiducial C/O ratio of 0.4 (see Table 6.B.1 and 6.B.1.2).

For the HCO^+ abundance, the chemical network presented in Leemker et al. (2021) is used. This is a small chemical network centred around HCO^+. This network does include the freeze-out and thermal desorption of H_2O, but not that of CO. As the only carbon-bearing molecules in this network are CO and HCO^+, this network is only run for the models with C/O < 1. This network is evolved using the density and temperature structure of the DALI model together with initial CO and H_2O abundances to match the C/O ratio.

6.2.6 Raytracing

The synthetic ALMA observations are produced using the raytracer in DALI. The level populations without assuming local thermodynamical equilibrium (LTE) are calculated using the collisional rate coefficients for ^{12}CO, ^{13}CO, $C^{18}O$, $C^{17}O$, C, HCN, CN, C_2H, NO, and HCO^+ in the LAMDA database[2] (Launay & Roueff 1977; Johnson et al. 1987; Roueff & Le Bourlot 1990; Schroder et al. 1991; Staemmler & Flower 1991; Schöier et al. 2005; Dumouchel et al. 2010; Lique et al. 2010; Yang et al. 2010; Spielfiedel et al. 2012; Denis-Alpizar et al. 2020; Ben Khalifa & Loreau 2021). An overview of the investigated transitions is presented in Table 6.A.1. The observed C_2H and NO data cover two respectively three lines that are blended with themselves. Therefore, these two and three transitions were raytraced and added assuming the emission is optically thin. Finally, all synthetic image cubes are convolved to a beam matching that of the observations.

6.2.7 The fiducial model

Thermo-chemical models are not expected to reproduce the observed line emission within the uncertainty of the data as the predicted molecular line emission depends both on the abundance of a certain molecule as well as the temperature of the emitting layer. The parameter studies of the DALI thermo-chemical code show a

[2] `https://home.strw.leidenuniv.nl/~moldata/`

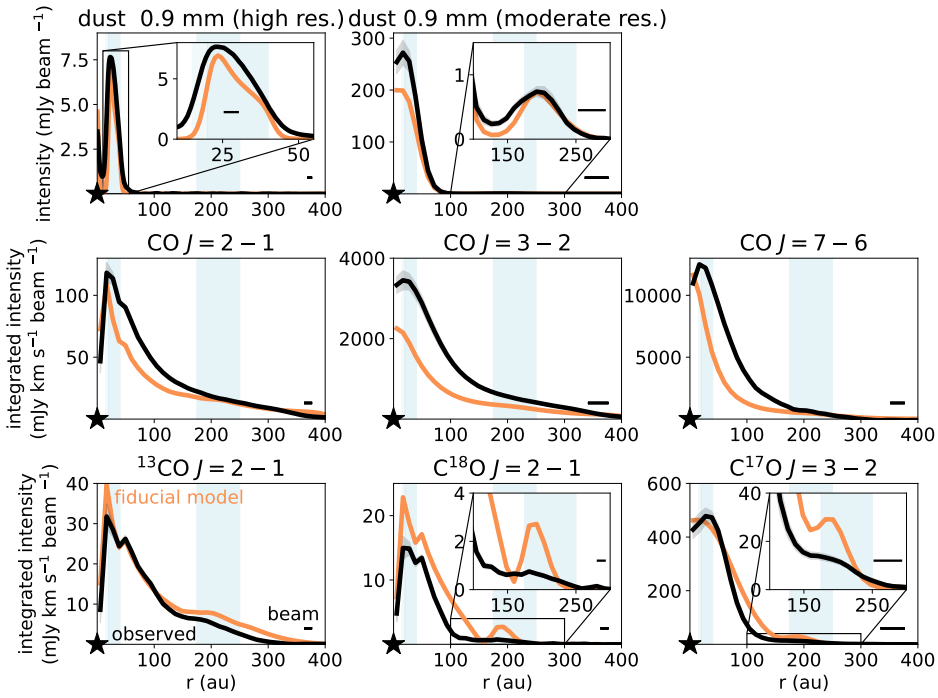

Figure 6.3: Azimuthally averaged radial profiles of the dust and CO isotopologue emission observed in the HD 100546 disk (black) together with the fiducial model (orange). The beam is indicated with the horizontal bar in the bottom right corner of each panel. The continuum observations are taken from Pineda et al. (2019) (high resolution 0.9 mm continuum), Booth et al. (2023a) (moderate resolution 0.9 mm continuum), the CO, ^{13}CO, and C^{18}O $J = 2 - 1$ transitions are first presented in Pérez et al. (2020) and Wölfer et al. (2023a), the CO $J = 7 - 6$ transition is presented in Wölfer et al. (2023a), and the CO $J = 3 - 2$ and C^{17}O $J = 3 - 2$ transitions are presented in Booth et al. (2023a).

factor of $\sim$2 difference in line flux due e.g. uncertainties in reaction rates in the chemical networks (Bruderer et al. 2012; Bruderer 2013). Therefore, a model is expected to reproduce the data within a factor of 2$-$3 in general (Kama et al. 2016; Sturm et al. 2023a). Instead of matching the observed line intensities within the uncertainty of the data, we look for trends in the abundances and line intensities for a range of key parameters such as gap depth and chemical composition.

The key feature of the emission in the HD 100546 disk is that all molecular rings are co-spatial with the dust rings, whereas the CO isotopologue emission appears smooth. The only structure seen in the CO isotopologue emission is a central gas cavity and a weak shelf of C^{18}O and C^{17}O emission extending from 150 au to 250 au (see insert in the bottom middle and right corner of Fig. 6.3). Therefore, the aim of the fiducial model is not to fit the CO isotopologues perfectly. Instead, the aim of the fiducial model is to provide a basis that roughly fits the continuum

and the CO isotopologues and explore under what conditions the molecular rings coincide with those seen in the continuum emission. The observations of the outer molecular rings are all consistent with emission originating from close to the midplane (Booth et al. 2023a). Therefore, the fiducial model has a low flaring index of $\psi = 0$ and a low scale height of $h_c = 0.1$ at the characteristic radius. A comparison of our fiducial model with those presented in Pirovano et al. (2022) and Keyte et al. (2023) is shown in Fig. 6.B.1, where the main differences are that the model presented in this work is significantly less flared than those presented in Pirovano et al. (2022) and Keyte et al. (2023), and has a gas cavity at < 15 au that is not present in Keyte et al. (2023). An overview of the parameters of the fiducial model is presented in Table 6.B.1.

The gas and dust density, temperature, and UV field in this model are presented in Fig. 6.2. The midplane gas density inside the gap drops down to a low value of 10^7 cm^{-3} at 250 au, which is too low for the gas and dust to be thermally coupled in the midplane. Therefore, the gas temperature at these locations is colder than that of the dust. The small dust follow the gas outside the gas cavity at 15 au. The large dust is only seen in the two dust rings at $20-40$ au and $175-200$ au. A steep drop in the UV field is seen at $z/r = 0.2$. This layer also roughly separates the warm surface layer of the disk from the layers below 50 K closer to the midplane. This flat model intercepts less UV radiation from the central star than more flared models, which causes a small amount of CO freeze-out in the outer dust ring.

The resulting emission of the mm-dust and the CO isotopologues is presented in Fig. 6.3. The top row presents the fits of the fiducial model to the dusty inner disk and the dust ring from $20-40$ au seen in the high resolution continuum (left panel) as well as the much weaker dust ring at $175-250$ au seen at moderate spatial resolution (middle panel; Pineda et al. 2019; Booth et al. 2023a). The weak outer continuum ring is not seen in the left panel due to the high spatial resolution and small maximum recoverable scale (26 au in radius) of that dataset.

The gas density structure is improved by including a 15 au gas cavity that is seen in the high spatial resolution $J = 2-1$ transition of ^{12}CO, ^{13}CO, and C^{18}O presented in the middle and bottom left panels in Fig. 6.3 (Pérez et al. 2020; Wölfer et al. 2023a). To match these data, the gas density inside the gas cavity is lowered by a factor of 10^{-5} and between the gas (15 au) and dust cavity (20 au) by a factor of 10^{-2}. Outside the gas cavity, the ^{13}CO, C^{18}O, and C^{17}O emission matches that of the observations (Pérez et al. 2020; Booth et al. 2023a; Wölfer et al. 2023a), with an especially close match being achieved for the ^{13}CO and C^{17}O emission. The ^{12}CO $J = 3-2$ and $J = 7-6$ emission presented in Booth et al. (2023a) and Wölfer et al. (2023a) is underproduced by at most a factor of ~ 2 likely due to the gas temperature that is slightly too low in this flat model. However, the main focus of the fiducial model is on the rarest CO isotopologues (C^{18}O and C^{17}O), the dust rings and the molecular line emission.

The lack of mm-dust between the two dust rings in the HD 100546 disk may be due to a massive planet carving a gap in the disk (Pinilla et al. 2015; Fedele et al. 2021; Pyerin et al. 2021). Therefore, the gas density in this region may be lower than in a full disk model. This is explored in Fig. 6.B.2 and we find that CO isotopologue emission is consistent with a shallow gas gap where the gas is

depleted by at most one order of magnitude, assuming that the gas and dust gap have the same widths.

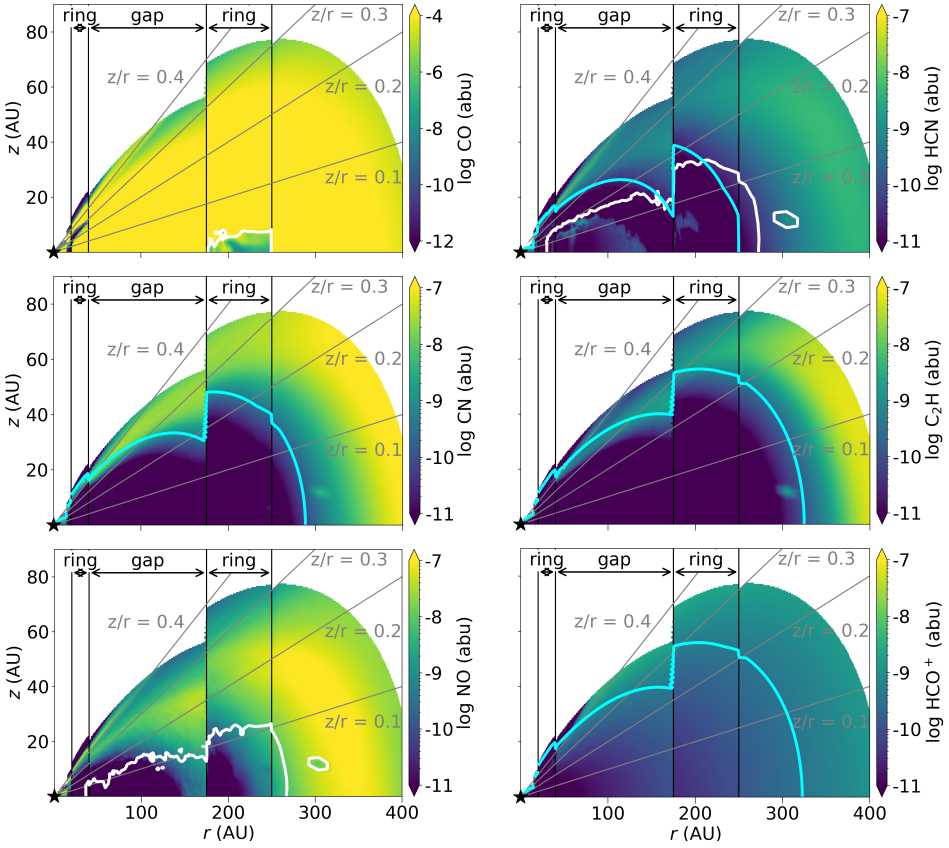

Figure 6.4: 2D abundance maps of CO, HCN, CN, C_2H, NO, and HCO^+. Note that the CO abundance is shown on a different colorscale. The white contour indicates the snowline of CO, HCN, and NO in their respective channels. The blue contour shows the critical density assuming a temperature of 50 K. Only the regions with a gas number density above 10^5 cm^{-3} are shown. As the CO and NO critical densities are lower than this, those contours are not shown in the respective panels.

6.3 Results

The HD 100546 disk is one of the few objects where the observed HCN, CN, C_2H, and HCO^+ emission lines are seen in two concentric rings that are co-spatial with the continuum emission (see Booth et al. 2023a, or Fig. 6.5 in this work). In contrast to the IRS 48 and PDS 70 disks, however, this disk does not have a deep gap between the two dust rings (see Sect. 6.2.7). The abundance structure and emission of HCN, CN, C_2H, NO, and HCO^+ are presented in this section, where

we explore their sensitivity to the model parameters to better understand what shapes their emission.

6.3.1 2D abundance maps

The 2D abundance structures of the molecules of interest, HCN, CN, C_2H, NO, and HCO^+, are presented in Fig. 6.4 together with the CO abundance for reference. The abundances are calculated with respect to the total hydrogen density: $n_h = n(\mathrm{H}) + 2 \times n(\mathrm{H_2})$. All of these molecules except CO follow the same global morphology: a surface layer with a high abundance that extends from the inner dust ring or the gap out to the outer disk at 400 au where the layer moves down to the midplane. Additionally, HCN and CO are abundant at lower disk layers and the NO and HCO^+ layers extend to the disk midplane from $\sim$ 150 au outward. The CO is abundant throughout the entire disk except in the surface layers where CO is photodissociated and in the midplane in the outer dust ring where CO is frozen out onto the dust grains.

HCN, CN, C_2H, and NO are sensitive to the UV field. The UV radiation in the surface layer forms vibrationally excited molecular hydrogen, $H_2{}^*$. This molecule then reacts with N to form NH that then reacts with C^+ to form CN^+ that is converted to CN and HCN. Additionally, a pathway through CH and N to form CN is also seen in this region. As the UV field only penetrates the surface layers of the disk, the HCN, CN, and C_2H are also constrained to this layer and thus reside in a layer where the number density of molecular hydrogen is below the respective critical densities (cyan contours in Fig. 6.4). The HCN molecule is not only abundant in a surface layer at $z/r > 0.2$; a secondary layer formed through different chemical reactions exists around a scale height of 0.1. Here, the HCN is mainly formed through a reaction of atomic carbon with H_2 to form CH_2 through radiative association which then reacts with O and N to form CO and HCN. As this layer is below the HCN snow surface (white contour in Fig. 6.2), this HCN quickly freezes-out.

Somewhat deeper in the disk at $z/r = 0.2$ NO is abundant. The NO is mainly formed through the reaction of NH with O with a minor contribution of the reactions of OH and N ($< 10\%$). The NO layer lies somewhat deeper in the disk than that of HCN, CN, and C_2H due to the destruction of NO by atomic carbon and nitrogen that (re)forms CO, CN, and N_2. At lower layers below $z/r = 0.1$, NO quickly freezes-out onto the dust grains as the NO snowline is located at a scale height of 0.1 in the dust gap and the outer dust ring. The thin NO layer at $z/r = 0.4$ is due to the photodissociation of water forming OH (see also Leemker et al. 2023).

Finally, the HCO^+ abundance is high at $\sim 10^{-9}$ in the highest layers of the disk above $z/r = 0.3$ due to the high ionisation enhancing the $H_3{}^+$ abundance in this region. In addition to ionisation, the HCO^+ ion traces the water snowline: a high HCO^+ abundance is only seen outside the water snowline where water cannot destroy HCO^+ (Phillips et al. 1992; Bergin et al. 1998). The water snowline in this model is located at the outer edge of the gas cavity at 15 au. Therefore, the HCO^+ abundance at larger radii scales as $\sqrt{\zeta_{\mathrm{c.r.}}/n_{\mathrm{H_2}}}$ with a weak dependence on

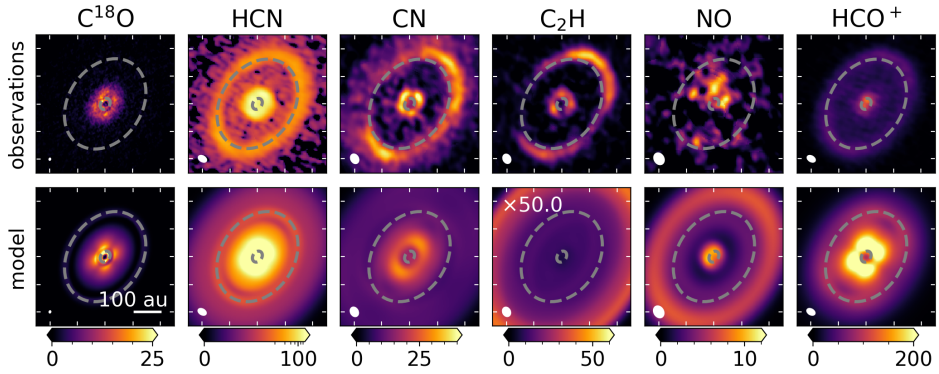

Figure 6.5: Integrated intensity (moment 0) maps of $C^{18}O$, HCN, CN, C_2H, NO, and HCO^+ emission in the HD 100546 disk. The top row presents the observations (Booth et al. 2023a) and the bottom row the predictions of the fiducial model. All intensities are in mJy km s^{-1} $beam^{-1}$. The dotted grey ellipses indicate the dust rings seen in the high spatial resolution (inner ring) and in the moderate spatial resolution (outer ring) 0.9 mm continuum. The tickmarks on the panels are spaced by 1", the horizontal bar in the bottom left panel indicates a 100 au scale. The HCN is shown on a logarithmic scale to highlight the weak outer ring and the modelled C_2H emission has been multiplied by a factor of 50. The beam of each of the observations is indicated with the white ellipse in the bottom left corner.

temperature (Leemker et al. 2021). This may overpredict the HCO^+ abundance outside the inner dust ring in this disk as cold, gas-phase water seen outside $\sim$ 40 au in this disk and water photodesorption is not included in the small chemical network (van Dishoeck et al. 2021; Pirovano et al. 2022).

Altogether, the 2D abundance structures of HCN, CN, C_2H, NO, and HCO^+ are dominated by a layer with a high abundance centred at $z/r \sim 0.2 - 0.3$. This layer is located at or above the critical density of HCN, CN, and C_2H, therefore, these molecules may not be in LTE. This is similar to the observed emitting layer of CO and higher than the layer of $z/r \leq 0.1$ that the HCN, CN, C_2H, and HCO^+ observations suggest (Booth et al. 2023a). The high abundance layer moves down slightly inside the gas gap due to the lower gas density, but apart from this, no clear jump in the abundance at the location of the outer dust ring is seen.

6.3.2 Integrated intensity maps

The integrated intensity (moment 0) maps of the data and the fiducial model are presented in Fig. 6.5. The modelled $C^{18}O$ emission reproduces the observations within a factor of two for most disk regions with the outer ring in $C^{18}O$ being more prominent in the model than in the data (see also Fig. 6.3, bottom row). For the other molecules on the other hand, the observed intensities or the double ringed profile are not reproduced. Only the modelled HCN and HCO^+ emission do show a hint of an outer ring at the location of the second dust ring and the C_2H and NO show a (weak) ring outside the outer dust ring.

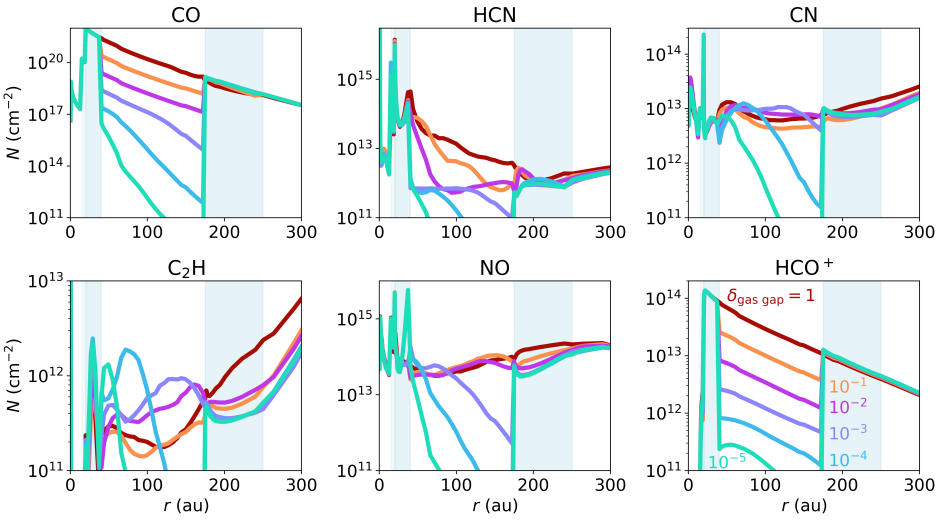

Figure 6.6: Column densities of CO, HCN, CN, C_2H, NO, and HCO^+ in the fiducial model with a C/O ratio and a gas gap depth of 1 (no gap; dark red), 10^{-1} (fiducial model; orange), 10^{-2} (pink), 10^{-3} (purple), 10^{-4} (blue), and 10^{-5} (very deep gap; light blue). The small dust density is dropped by the same factor in the gap as in the gas.

The inner ring that is observed in HCN and CN is reproduced by the model within a factor of ~ 2 but the observed C_2H ring at 40 au is not seen in the model. The modelled HCO^+ emission is ring-shaped in the inner disk with a ring at 60 au, whereas the data are centrally peaked at the spatial resolution of the observations. The intensity in the modelled ring is two times higher than what is observed at the central location.

The model predicts outer rings in HCN and HCO^+ that are only a factor of ~ 3 weaker and a factor of two brighter than what is observed, respectively. However, the model does not reproduce the outer ring in C_2H as the modelled ring is two orders of magnitude weaker and 170 au further out than seen in the data. Similarly, the observed outer ring in CN is not recovered by the model and the modelled NO emission is mostly seen just outside the inner dust ring and outside the outer dust ring whereas the observations show some emission between the two dust rings and possibly at the location of the outer dust ring. In summary, Fig. 6.5 shows that despite a good fit to the continuum and CO isotopologue emission, the model does not reproduce the observations of molecules other than CO isotopologues, especially for CN, C_2H, and NO. The chemical network used to calculate these abundances reproduces the CN, HCN, HNC, and C_2H emission in other protoplanetary disks within a factor of a few in general (e.g., Cazzoletti et al. 2018; Visser et al. 2018; Miotello et al. 2019; Long et al. 2021). Therefore, the difference between the model predictions and the observations in the HD 100546 disk are likely due to the physical structure of the disk rather than uncertainties in the chemical network.

6.3.3 A deeper gas gap

A possible solution to create double rings in the molecular line emission is to induce a deep gas gap between the two dust rings. The ^{12}CO emission does not show any evidence of a gas gap deeper than the fiducial depth of a factor of 10, neither does the C^{17}O where only a shoulder of emission extending out to $200 - 300$ au is observed (see Fig. 6.B.2). Still, a depletion of gas could affect the molecular line emission. Therefore, the effect of a deeper gas gap is investigated in this subsection. The small dust is assumed to follow the drop in the gas density.

6.3.3.1 Column densities

The effect of the depth of the gap between 40 and 175 au on the column density is presented in Fig. 6.6 where the column densities inside 250 au are smoothed in log space with a savgol filter in scipy over 10 points and a 3rd order polynomial to remove any artificial spikes due to low photon statistics in the model. The CO column density directly traces the drop in the gas density for gaps up to three orders of magnitude in gas density. For deeper gaps, CO photodissociation becomes important and the CO column density drops even faster than the gas density.

The HCO$^+$ column density directly follows that of the gas where a drop of two orders of magnitude in gas column density results in a one order of magnitude drop in the HCO$^+$ column density. The reason for this is that the HCO$^+$ number density outside the water snowline follows $n(\mathrm{HCO^+}) \propto \sqrt{\zeta_{\mathrm{c.r.}} \times n(\mathrm{H_2})}$, with $\zeta_{\mathrm{c.r.}}$ the cosmic ray ionisation rate and $n(\mathrm{H_2})$ the density of molecular hydrogen (see eq. B.6 in Leemker et al. 2021). Therefore, the HCO$^+$ column density in the gap is directly related to that of the gas.

The CN, C_2H, and NO show a different pattern than CO, but a similar pattern to each other, in their column densities when the gap depth is increased. For shallow to somewhat deep gas gaps ($\delta_{\mathrm{gas\ gap}} \sim 1 - 10^{-2}$) their column densities are independent of the gap depth within a factor of a few. For very deep gas gaps ($\delta_{\mathrm{gas\ gap}} \sim 10^{-4} - 10^{-5}$) a steep decrease in the column density is seen in the outer parts of the gap. The sharp peaks in the HCN, CN, C_2H, and NO column densities at the inner ring and cavity (15, 20, and 40 au) may be sensitive to the precise conditions in this region.

This behaviour can be understood from the 2D UV field and CN abundance which are presented in Fig. 6.7. Shown are the results for a shallow gap (10^{-1}) and two deep gaps (10^{-3} and 10^{-5}) . In left column, a shallow gas gap is present, but the CN is only abundant in a layer high above the midplane at $z/r = 0.3$ in the gap. Changing the amount of gas in this region only shifts this layer up or down, but it does not affect the column density greatly as the midplane abundance of CN is low. For a deep gas gap (middle and right columns), the UV field is more intense in the gap than in the model with a shallow gas gap. As CN is sensitive to the UV field, its abundance increases in the gap. The resulting CN column density is an interplay of an increase in the abundance that is most prominent at small radii, and a decrease in the gas column density that is most effective at large radii. This causes a peak in the CN column density that moves to smaller

radii of 75 and 50 au with deeper gaps of 10^{-4} and 10^{-5}, respectively. As C_2H and NO are also sensitive to the UV field, their abundances and column densities show the same qualitative behaviour. Especially for C_2H, the inward travelling peak in the column density is clearly visible at 160 au, 140 au, 70 au, and 50 au for $\delta_{\text{gas gap}} = 10^{-2}, 10^{-3}, 10^{-4}, 10^{-5}$, respectively.

The HCN column density always decreases or stays constant with deeper gaps due to the moderate HCN abundance in the midplane together with the high abundance in the surface layer. The component in the midplane slowly decreases up to a gap depth of 10^{-2}, lowering the HCN column density simultaneously. For deeper gaps, the midplane component of the HCN vanishes and the HCN column density steeply drops with gas density, similar to the pattern seen for CN, C_2H, and NO.

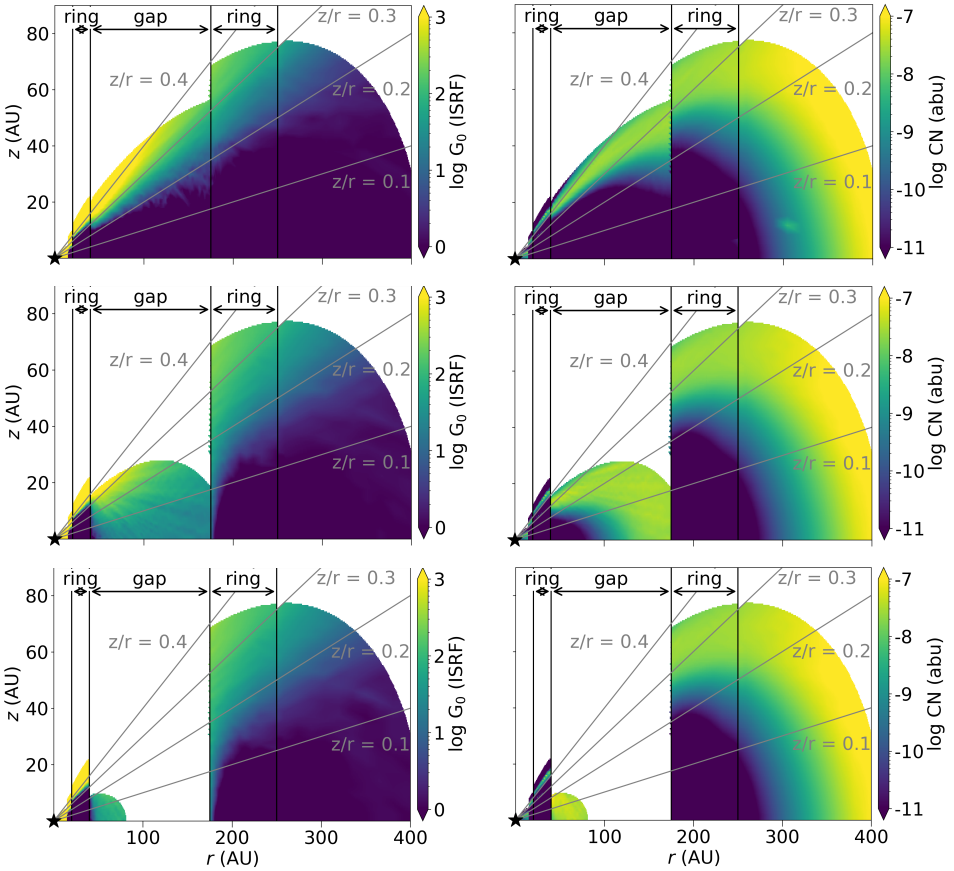

Figure 6.7: The UV field and CN abundance for different gas gap depth. From left to right: $\delta_{\text{gas gap}} = 10^{-1}$, 10^{-3}, and 10^{-5}. The top row shows the UV field in units of G_0 and the bottom row the CN abundance. Only the regions with a gas number density above 10^5 cm^{-3} are shown.

6.3.3.2 Emission maps

The integrated intensity (moment 0) maps for different gas gap depths are presented in Fig. 6.8 and Fig. 6.B.4. The fiducial model is presented on the second row and the moment maps are identical to those presented in Fig. 6.5 but on a different colorscale. In general, the molecular line emission shows ringed emission for all models that have some degree of gas depletion between the dust rings ($\delta_{\text{gas gap}} = 10^{-1} - 10^{-5}$). However, double rings are only seen for the models with a very deep gas gap ($\delta_{\text{gas gap}} = 10^{-4} - 10^{-5}$). These rings are typically located outside the dust rings instead of at the dust as seen in the observations. For example, the NO emission shows a very clear double ring for these models, but the outer ring is located at 300 au where no NO is seen in the data. The C_2H emission shows a ring of emission inside the gas gap that moves inwards with increasing gap depths following the corresponding C_2H column density. This effect is also seen in the CN and NO emission, although it is less pronounced. The NO emission just outside the inner ring is sensitive to a sharp peak in the column density and may be very sensitive to the conditions in this region. The remaining three molecules, $C^{18}O$, HCN and HCO^+ all show double ringed profile for all models with some gas depletion.

The model with a deep gas gap of 10^{-4} times less gas best reproduces the double ringed nature of the HCN, CN, and C_2H observations, whereas the model with a factor of ten more gas ($\delta_{\text{gas gap}} = 10^{-3}$) reproduces the diffuse HCO^+ emission between the dust rings better. The first model reproduces the morphology of the molecular line emission just outside the inner dust ring for CN and C_2H while also predicting a reasonable intensity for HCN. Additionally, this model reproduces the presence of an outer ring seen in HCN, CN, and HCO^+. The CO isotopologue emission on the other hand is best reproduced by a disk with a shallow gap of only 10^{-1} times less gas as the $C^{18}O$ emission in the gap is directly related to the drop in gas density.

6.3.3.3 Molecular column densities and line ratios

Ratios of column densities can give additional insights into the underlying processes as they are less sensitive to the absolute model results. The column density ratios of HCO^+/CO, C_2H/CO, CN/HCN, and CN/NO are presented in Fig. 6.9 for a model without a gas gap and models with gap depths up to 10^{-5}. The first three ratios increase with radius outside the outer gas cavity in the full gas disk model, whereas the CN/NO ratio first increases inside the dust gap, then slowly decreases up to the outer dust ring and then somewhat increases again. This is caused by the different radii where the CN and NO column densities peak in the disk. The HCO^+/CO and C_2H/CO ratios increase due to the increasing column density in HCO^+ and C_2H as that of CO smoothly decreases with radius. Finally, the increase in the CN/HCN ratio is driven by the decreasing column density of HCN.

When a gas gap is introduced, the ratios presented in Fig. 6.9 all increase compared to the model without a gas gap except for a disk with a gap of 10^{-1} and 10^{-2} times less gas where the CN/NO ratio stays roughly constant in the gap.

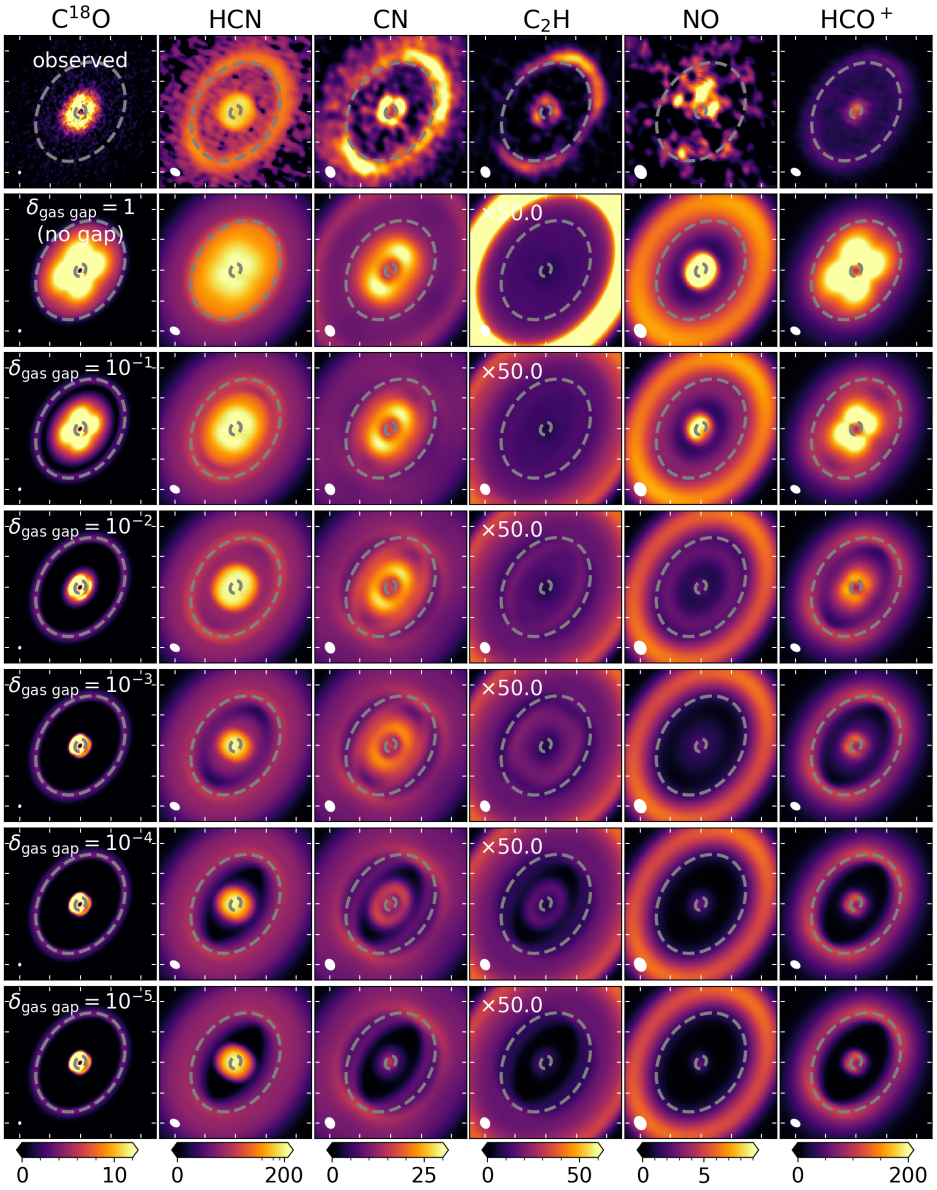

Figure 6.8: Integrated intensity (moment 0) maps in mJy km s^{-1} beam^{-1} for C^{18}O, HCN, CN, C_2H, NO, and HCO^+ from left to right. The different rows present the results for different depth of the gas gap with the gap depth ($\delta_{\text{gas gap}}$) indicated in the top of the left column. The HCN emission is shown on a logarithmic scale to highlight the weak outer ring. The beam is indicated in the bottom left corner of each panel and the tickmarks on the axes are spaced 1" apart.

The same trend is seen in the ratios for models with $\delta_{\text{gas gap}} = 1 - 10^{-2}$ of the corresponding molecular lines presented in Fig. 6.B.7. For deeper gas gaps, the line ratios become insensitive to the gas gap depths due to the finite resolution of the observations. This is because part of the bright emission in the rings leaks into the gap regions, causing these regions to be dominated by the rings for deep gas gaps. Altogether, the column density ratios of HCO^+/CO, C_2H/CO, and CN/HCN of show a strong dependence on the gas gap depth that is much weaker in the ratios of the emission lines.

6.3.4 Different C/O ratios

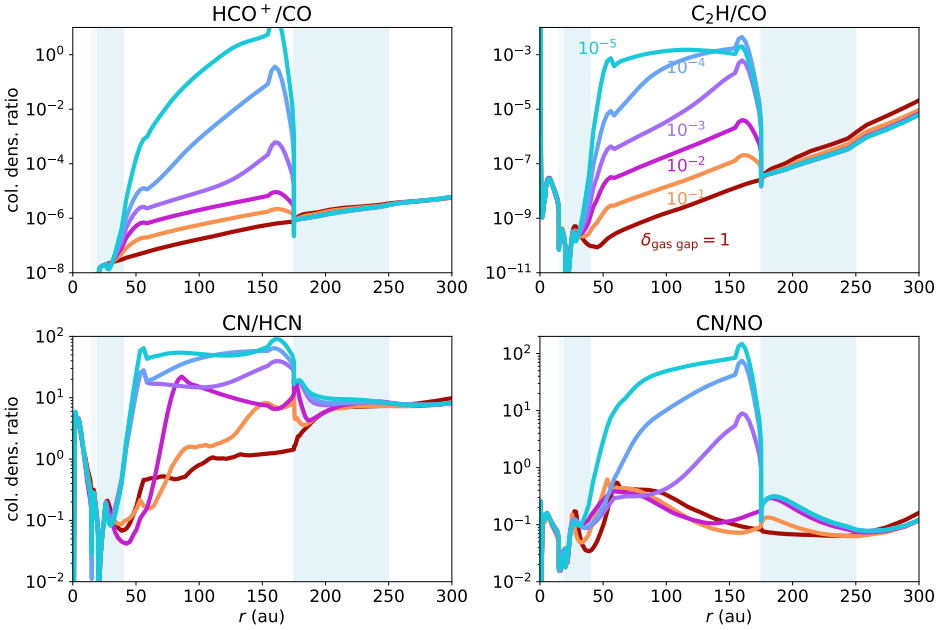

Figure 6.9: Column density ratios of HCO^+/CO (top left), C_2H/CO (top right), CN/HCN (bottom left), and CN/NO (bottom right) for different gas gap depths.

6.3.4.1 Column densities and emission profiles

The observed C_2H emission is two orders of magnitude brighter than predicted by the fiducial model. Observations in other disks show that the C_2H emission becomes significantly brighter when the C/O ratio of the gas exceeds 1 (e.g., Bergin et al. 2016; Miotello et al. 2019; Bosman et al. 2021b). In this section, the effect of an increased C/O ratio is explored in the fiducial model with a gas gap of $\delta_{\text{gas gap}} = 10^{-1}$. The 2D abundance maps for C_2H and NO are presented in Fig. 6.10. The 2D abundance maps in the top row are the maps for the fiducial model and are the same as those presented in Fig. 6.4. The middle and bottom

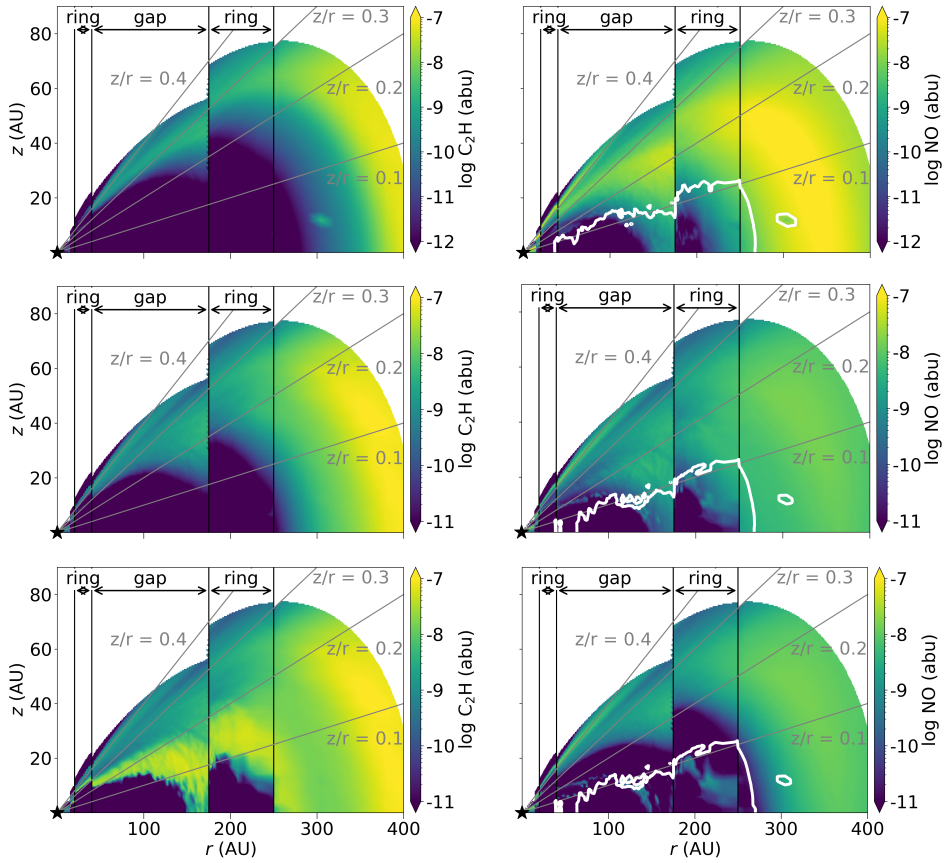

Figure 6.10: The C_2H (left column row) and NO (right column) abundance for different C/O ratios. From left to right: C/O = 0.4 (fiducial value), 0.99, and 1.01. Only the regions with a gas number density above 10^5 cm^{-3} are shown. The white contour indicates the NO snowline.

row show these maps for a C/O ratio just below one at 0.99 and just above one at 1.01. As the C/O ratio increases, the layer where C_2H is abundant moves down from $z/r = 0.3$ for C/O = 0.4 to $z/r = 0.2$ for C/O = 0.99 and then it jumps down to $z/r = 0.15$ for a C/O ratio that is only 0.02 higher at 1.01. The peak C_2H abundance in this layer also jumps from $\sim 2 \times 10^{-9}$ to 4×10^{-9} and to 7×10^{-8} for C/O = 0.4, 0.99, and 1.01, respectively. A similar trend is seen for HCN, CN, and C.

The NO abundance shows the opposite behaviour as NO is expected to become less abundant when the C/O ratio is high. This is also seen in the 2D abundance maps as the NO abundance quickly decreases if the C/O is increased from 0.4 to 0.99 by removing water. As the C/O ratio further increases the NO layer splits into two regions around $z/r = 0.05$ below its snow surface and one at $z/r = 0.2 - 0.3$. HCO^+ and CO both carry one oxygen atom and one carbon atom and are therefore not as sensitive to the C/O ratio. The column densities for these molecules for C/O ratios between 0.4 and 1.2 are presented in Fig. 6.B.6 in Appendix 6.B.3.3.

The step-like behaviour of the CN and C_2H abundance is also seen in the azimuthally averaged integrated intensity profiles presented in Fig. 6.11. If the C/O ratio increases from 0.99 to 1.01, the CN and C_2H integrated intensities increase by a factor of a few to one order of magnitude and by to two orders of magnitude in the gap, respectively. The C/O ratio does change the integrated intensity across the disk, but the locations of the CN and C_2H peaks remain around those seen in the data except for a large peak at $300 - 400$ au seen in C_2H. Interestingly, the observed C_2H emission falls between that predicted by models with C/O = 0.99 and 1.01, possibly indicating a C/O ratio in the rings that is very close to 1.00.

The HCN emission only shows a double peak profile for the models with C/O = 0.4 and 0.8 as the column density inside the gap increases faster with increasing C/O than that just outside the gap. The model with a C/O of 0.8 matches the intensity in the outer dust ring particularly well whereas in the model with C/O = 0.4 matches the inner ring within a factor of ~ 2.

The top left panel in Fig. 6.11 presents the azimuthally averaged radial profile of the observed [C I] emission in the HD 100546 disk. Unlike the HCN, CN, C_2H, and HCO^+ emission, the [C I] does not show a double peaked profile at the dust rings. This could partially be due to the small maximum recoverable scale of 2" ($\sim$ 108 au in radius), filtering the emission at larger distances. Therefore, the model may overpredict the observed line intensity outside this radius. Inside $\sim$ 108 au, the fiducial model underpredicts the emission of atomic carbon by an order of magnitude. The only model that recovers the observed [C I] intensity up to 150 au is the model with a C/O of 1.2.

The effect of the C/O ratio on the NO emission is that the NO peak moves inwards from 300 au to $\sim$ 40 au. The high intensity at small radii is due to some additional NO at $z/r = 0.1 - 0.2$ in the models with C/O > 1. The intensity in the outer disk decreases with increasing C/O ratio due to the lower abundance.

In summary, increasing the C/O ratio increases the predicted intensity for [C I], HCN, CN, C_2H, and NO inside 100 au and for NO it decreases the intensity outside 100 au. The observed emission lines are reproduced by different C/O ratios for

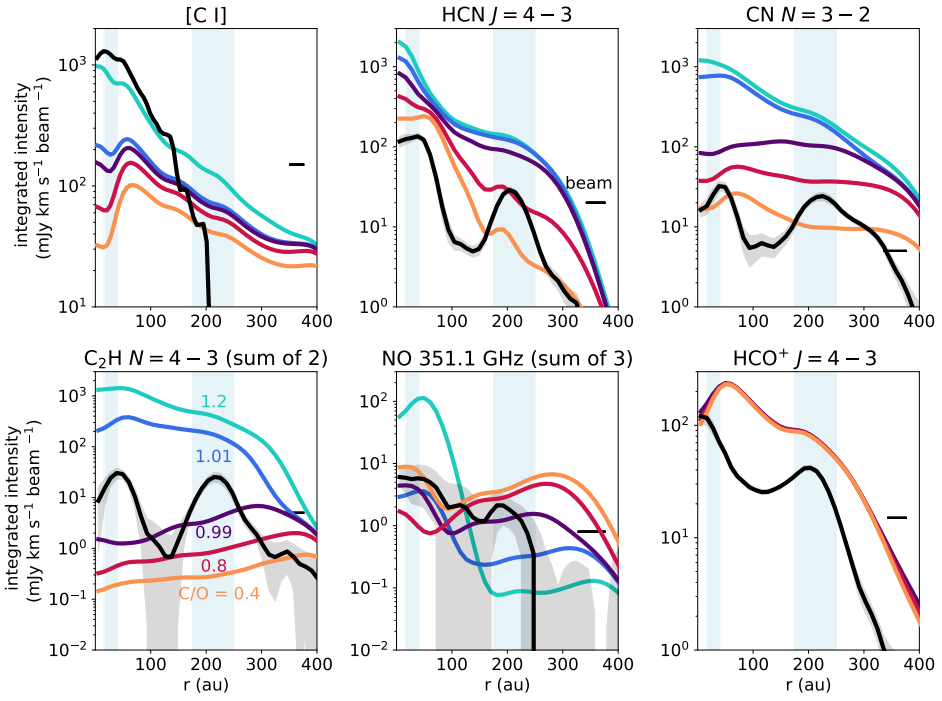

Figure 6.11: Azimuthally averaged integrated intensity of the molecular line emission for different C/O ratios in a model with a gas gap depth of 10^{-1}. The black line indicated the observed intensities.

each molecule. For example, the region inside 150 au is best reproduced by C/O = 1.2 for [C I], but this overpredicts the CN and C_2H emission by more than an order of magnitude. At the location of the outer dust ring, the cyanides (HCN and CN) and NO are compatible with a C/O ratio of 0.8, but the C_2H requires a C/O ratio very close to 1 ($0.99 < C/O < 1.01$).

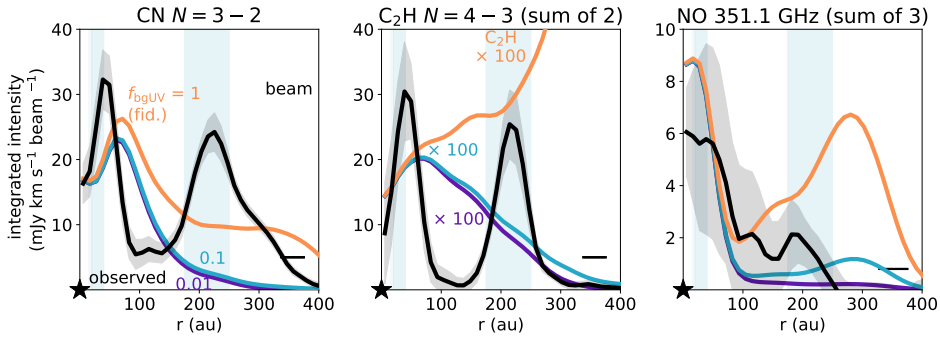

Figure 6.12: Azimuthally averaged integrated intensity of the CN, C_2H, and NO for different background UV radiation fields. The modeled C_2H emission is increased by a factor of 100 to show it on the same scale as the observations.

6.3.4.2 Column density and emission line ratios

To eliminate some of the uncertainties of comparing absolute modelled intensities to the observed ones, the column density and line ratios of $HCO^+/C^{17}O$, $C_2H/C^{17}O$, CN/HCN, and CN/NO are presented in Appendix. 6.B.3.3. The latter three column density ratios all increase in most disk regions with increasing C/O due to the enhancement of C_2H and CN, and the decrease of NO. In particular, the CN/NO ratio outside 100 au and the $C_2H/C^{17}O$ in the entire disk are sensitive to small changes in the C/O. Comparing the observed emission line ratios to the modelled ones shows that the C/O needs to be very close to 1.00 as the $C_2H/C^{17}O$ ratio for C/O = 0.99 underpredicts the observed value and that of C/O = 1.01 overpredicts the observations. The CN/NO line ratio only traces the C/O ratio for $r > 175$ au, and is therefore not a good tracer of the C/O in the disk.

6.3.5 Background UV

One striking feature that most of the models presented here show is that the CN, C_2H, and NO emission are too bright outside the outermost dust ring. This raises the question if the modelled external UV field is too strong as all of these molecules at least partially trace the UV field. The models assume that the external UV field is 1 G_0, the mean UV field in the interstellar medium. However, HD 100546 is an isolated star with a tenuous envelope may result in a lower external UV field (Grady et al. 2001).

The effect of a lower UV field on the CN, C_2H, and NO column density is presented in Fig. 6.B.11. Lowering the background UV field by a factor of ten decreases the CN and C_2H column densities by that same factor outside the outer dust ring. The NO decreases by a factor of 5 in that same region. This is also reflected in the azimuthally averaged radial intensity profiles presented in Fig. 6.12. The shelf of CN and the peak of C_2H at 375 au are not visible for the lowered background radiation fields, creating a ring of emission at the location of the outer dust ring. The effect of a lower background UV field on the [C I], HCN, and HCO^+ emission is small.

In particular, a lower background UV radiation field more closely reproduces the double peak profile of the C_2H emission, with both peaks having a similar intensity. The C_2H intensities in these models is a factor of 200 lower than what is observed for C/O = 0.4. Additionally, the NO emission in the outer disk is not overpredicted if the background radiation field is lowered. Overall, a lower background UV field seems to improve the comparison with observations outside the outer dust ring.

6.3.6 Flaring

The observations of HCN, CN, C_2H, and HCO^+ show two emission rings that are concentric around the position of the star. This indicates that these molecules emit from a layer close to the disk midplane ($z/r \leq 0.1$, Booth et al. 2023a) as an elevated layer would shift these rings w.r.t. the position of the star. Such an offset is indeed seen in the models for CN. Figure 6.13 presents this with the light and dark blue ellipses for different flaring indices of the disk. The ellipses indicate the projected location of the peak CN number density at the inner rim of the outer dust ring. For the two flattest models ($\psi = -0.1$ and 0) the CN at $r = 175$ au peaks at $z = 55 - 53$ au whereas for the two more flared models ($\psi = 0.1$ and 0.2), the CN peaks at a height of $66 - 68$ au at $r = 176$ au. These ellipses trace two rings in the CN emission in the moment 0 maps. These two rings increase and move slightly further apart with increasing flaring index, tracing the height where the CN is abundant. As this height only changes by ~ 10 au between a very flared and a close to flat disk, flaring alone cannot explain the observed emitting heights. However, the emission in the moment 0 map is not only depends on the vertical structure but also on the density and temperature. Observations of $C^{18}O$ in the Elias 2-27 disk show a ring that is close to being centered at the position of the star. Yet the $C^{18}O$ channel maps show that the emitting surface is flared, with $z/r \sim 0.2$ (Paneque-Carreño et al. 2021). Therefore, deriving the emitting height from integrated intensity maps may hide part of the true vertical structure of the disk. The column density and radial emission profiles for other molecules are presented in Appendix 6.B.5.

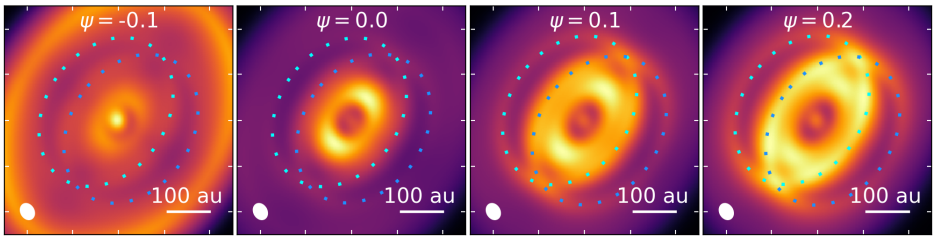

Figure 6.13: Moment 0 maps of the CN emission for models with different flaring indices $\psi = -0.1$ to $+0.2$. The light and dark blue ellipses indicate the projected location at which the modelled CN number density peaks at the inner rim of the outer dust ring, which corresponds to $z = 53 - 68$ au. The panels are shown on an individual colorbars for clarity.

6.4 Discussion

Correlations between the radial structures in the dust and gas could point to a common origin such as massive planets that are carving gaps in disks or to the sublimation of ices as seen in the IRS 48 disk (van der Marel et al. 2021b; Booth et al. 2021b; Brunken et al. 2022; Leemker et al. 2023). The observations in the HD 100546 disk show a clear correlation between the dust rings and the HCN, CN, C_2H, and HCO^+ emission suggesting a direct relation between the structures in the gas and the dust. However, the rare CO isotopologue emission, tracing the CO column density, does not show the same double ringed structure. In this work, we used thermochemical models to investigate under what conditions molecular rings are co-spatial with the dust rings.

6.4.1 Radial structures

6.4.1.1 CO isotopologues, HCO^+, and HCN

The thermochemical models spanning a range of gas gap depth ($\delta_{\text{gas gap}} = 1{-}10^{-5}$) show that three molecules directly respond to a the depletion of gas in the gap: CO isotopologues, HCO^+, and HCN. Comparing the modelled CO isotopologues to the observations shows that a shallow gas gap ($\delta_{\text{gas gap}} = 10^{-1}$) is needed as a deeper gas gap creates a gap in the emission that is not seen in the observations. A double ring is seen in HCN and HCO^+ if the modelled gas gap is at least two orders of magnitude deep (or one order of magnitude if the disk is viewed face-on due to projection effects, see Fig. 6.B.5 in Appendix 6.B.2.2). Interestingly, despite the correlations seen in the models, no general correlation is observed in the MAPS sources between the HCN and HCO^+ rings and the dust and only a weak ($\sim 3\sigma$) correlation is seen between the CO isotopologue emission and the dust.

The trend in the HCO^+ and CO isotopologues across the gas gap is also seen in other modelling works. Modelling of HCO^+ across a gas gap outside the CO snowline predicts that the ratio of the HCO^+ to the total gas column density

increases when a gas gap is introduced (Alarcón et al. 2020; Smirnov-Pinchukov et al. 2020). A difference in the model predictions is seen for the model with only a dust gap and no gas gap ($\delta_{\text{gas gap}} = 1$). This model presented in Smirnov-Pinchukov et al. (2020) shows an increased HCO^+/CO column density ratio in the dust gap whereas this is not seen in the models presented in this work (Fig. 6.9). A possible cause for this is that the gap in Smirnov-Pinchukov et al. (2020) is located outside the CO snowline. Part of the CO ice desorbs and reacts to form HCO^+, boosting the HCO^+ column density in their model. This is not seen in our models as CO is abundant throughout the disk instead of just in the dust gap.

6.4.1.2 CN, C_2H, and NO

The other modelled molecules follow a more intricate relation with the gas gap depth. Modelling of the HD 100546 disk shows that the locations of the rings seen in CN, C_2H, and NO are set by an interplay of gas column density between the two dust rings, and the resulting UV field. A deeper gas gap results in a lower gas column density and a higher UV field, which moves the peak CN, C_2H, and NO column density to smaller radii with increasing gap depths. Yet, the column density of these molecules is mostly insensitive to the gas gap depths for gaps shallower than $\delta_{\text{gas gap}} \sim 10^{-4}$. Only for the deepest gaps of $\delta_{\text{gas gap}} = 10^{-4}-10^{-5}$, the rings in CN, C_2H, and NO are close in radius to those seen in the dust.

For shallower gaps, the CN, C_2H, and NO rings peak at various radii both inside (CN, C_2H) and outside (NO) the dust rings and do in general not coincide with the dust rings or each other. Additionally, the inner and outer rings of a particular molecule are predicted to have very different intensities. This is similar to the results of the MAPS program which observed CN and C_2H and found no general and significant correlation between structures in the dust and in the molecular line emission in four out of five disks, despite some overlapping features (Law et al. 2021a; Jiang et al. 2022). For the models with a gap of $10^{-1} - 10^{-3}$, the C_2H is predicted to peak inside the dust gap, similar to what is seen in the MWC 480 disk, the only MAPS disk where gas structures other than CO isotopologue emission do correlate with the dust and in the AS 209 disk (Alarcón et al. 2021). The location of the inner CN ring is only sensitive to gas gap depth if the gap is depleted by five orders of magnitude in gas. Therefore, chemistry is the main driver of the ring locations for shallow gas gaps.

In summary, the radial locations of the rings seen in the HD 100546 disk cannot be explained by a single gas gap depth as the CO isotopologue emission, HCN, and HCO^+ are best reproduced by a shallow gap ($\delta_{\text{gas gap}} = 10^{-1} - 10^{-2}$), whereas the double ring in CN and C_2H is only reproduced for a deep gas gap of $\delta_{\text{gas gap}} = 10^{-4} - 10^{-5}$, partially due vertical structure of the disk. Unlike HD 100546, the PDS 70 and IRS 48 disk both have a deep gas cavity just inside the molecular rings, forcing the line emission to be co-spatial with that of the dust. Therefore, if a physical gap is present in a disk, for example due to a massive planet, the molecular rings are likely also physical rather than chemical rings.

6.4.2 Chemistry in the rings and gap

In addition to physical rings in the disk density structure, chemical rings can also affect the observed emission. The chemistry across the gap may vary due to e.g., thermal and non-thermal sublimation of the ice mantles on the dust and UV shielding by small dust grains.

Water ice is likely present on the dust grains in the gap between the two dust rings in the HD 100546 disk (Honda et al. 2016). Photodesorption of this water ice could explain the gas-phase water seen from just outside the inner dust ring (starting from $35 - 40$ au) to $\sim 300 - 400$ au (Du et al. 2017; van Dishoeck et al. 2021). The outer radius is not well constrained as the line profile that is used to constrain the emitting location is most sensitive to the inner radius rather than the outer radius (priv. comm. with M. R. Hogerheijde). Additionally, the line profile does not show evidence for a jump in the H_2O abundance at the location of the outer dust ring. Modelling of the cold water lines shows that gas-phase water has an abundance of 3×10^{-9} in the outer disk ($\sim 40 - 300$ au, Pirovano et al. 2022). Photodesorption of water ice is not included in the network used to predict the HCO^+ abundance in this work. As HCO^+ is destroyed by gas-phase water, the predicted HCO^+ abundance and emission are thus overestimated in the gas gap and also at larger radii out to 300 au. The difference between the modelled HCO^+ emission in the gap and the observed intensity could thus be due to this effect. As the gas gap does not contain large grains, water ice must be present on small grains.

Another mechanism that could lead to the rings seen in HCN, CN, C_2H, and HCO^+ and the detection of NO is grain surface chemistry. The temperature structure of the fiducial model suggests that the outer dust ring is sufficiently cold to have some HCN, CN, C_2H, NO, and CO freeze-out (see Fig. 6.4). Chemical networks including grain surface chemistry predict that the CO ice can be hydrogenated to H_2CO and CH_3OH, two molecules that are detected at this location in the disk (Walsh et al. 2014b; Booth et al. 2021c, 2023a). As the outer dust ring is too cold for thermal desorption of methanol, a non-thermal desorption processes could lead to a higher abundance. This process could also somewhat enhance the gas-phase abundance of HCN and NO by $10^{-3} - 10^{-4}$ times their ice abundance as both of these molecules have significant ice abundance ($> 10^{-7}$) in that region. The high NO abundance in the IRS 48 disk may have an origin in the ice (Leemker et al. 2023). C_2H and CN on the other hand do not have a high abundance in the ice and these emission rings thus require a different origin such as gas-phase formation or sublimation of larger molecules that form CN and C_2H after sublimation.

The sublimation of ices could also be reflected in the gas-phase C/O ratio as most ices are oxygen rich. The $C_2H/C^{17}O$ ratio is the most sensitive to the C/O ratio of the ratios investigated in this work. The CN/NO ratio has been suggested as a tracer of the gas-phase C/O ratio (Hily-Blant et al. 2010b; Daranlot et al. 2012; Le Gal et al. 2014). However, the models presented in this work show that the relation between CN/NO and C/O is more complicated than this. The reason for that is that a secondary layer of NO appears for C/O ratios larger than 1.

Our models suggest that the C/O ratio in the dust rings needs to be elevated from 0.4 to 0.8-1 to reproduce the HCN, CN, and C_2H emission in the dust rings, while the C/O in the gas gap is roughly consistent with the fiducial value of 0.4. The C/O in the rings is somewhat higher than the C/O of 0.5 derived from CS and SO by Keyte et al. (2023). In particular, the C_2H emission is very sensitive to the C/O ratio, consistent with what is found in earlier works (e.g., Bergin et al. 2016; Miotello et al. 2019; Bosman et al. 2021b). Additionally, the bright C_2H emission without having a deep gas gap points to an elevated C/O as also suggested in the AS 209 disk (Alarcón et al. 2021). The C_2H emission at the outer dust ring in HD 100546 could be due to freeze-out of CO and other oxygen bearing molecules in this region leading to a high C/O ratio (Öberg et al. 2011; van der Marel et al. 2021c, and Fig. 6.4). Two other mechanisms that could lead to an elevated C/O ratio are photoablation of carbonaceous grains and destruction of CO by He^+ (e.g., Bergin et al. 2014; Anderson et al. 2017; Klarmann et al. 2018; Bosman et al. 2021b). The latter process is included in the chemical network. The low C_2H emission could indicate that the cosmic ray ionisation rate or the X-ray flux are higher than modelled in this disk. The spatial overlap between the dust rings and the C_2H emission suggests that destruction of carbon grains could contribute to the elevated C/O ratio. Instead of an enhancement in the C/H ratio, the O/H ratio could also be suppressed by, for example the freeze-out of oxygen bearing molecules such as CO and methanol. As the C/H and O/H ratios in the HD 100546 photosphere are consistent with the Solar values, the increase in the C/O ratio in the disk is likely local (Kama et al. 2016).

HCO^+ not only traces the desorption of water, it is also sensitive to the ionization in the disk (e.g., Aikawa & Herbst 2001; Cleeves et al. 2015b). The observed column density ratios of HCO^+/CO in the MAPS disks increases with radius or stays roughly constant at $\sim 10^{-6} - 10^{-4}$ (Aikawa et al. 2021). The general trend of an increasing ratio with radius is recovered by our models, but the observed values require a gas gap depth of $\sim 10^{-2} - 10^{-4}$. Comparing this to the HD 100546 disk shows that either the gas gap is shallow ($\delta_{\text{gas gap}} = 1 - 10^{-1}$) for the outer half of the gap, or that the ionisation rate in the modelled gap is too high.

The ratio of CN/HCN, tracing the UV indicates that the gap in HD 100546 needs to be $10^{-1} - 10^{-2}$ deep (see Fig. 6.B.7). Radial variations in the CN/HCN column density ratio likely trace radial variations in the UV field due to changes in the dust density structure due to enhanced HCN photodissociation compared to CN photodissociation (Bergner et al. 2021). The models presented in this work show a similar trend where the CN/HCN column density ratio peaks inside the gas gap and decreases in the outer dust ring (see Fig. 6.9). Similarly, this ratio has a low value of a few 10^{-2} in the inner dust ring where the small dust surface density is two orders of magnitude higher than that in the outer dust ring (see Fig. 6.1). The model without a gap in the gas and small dust grains but with a gap in the large dust grains does not show a peak in the CN/HCN column density ratio in the gap, indicating that this ratio is primarily sensitive to the small dust grains that have a larger opacity in the UV than the large dust grains.

In summary, the rings seen in the HD 100546 disk likely have a chemical origin as the gas density structure alone cannot explain the observed molecule rings.

The C/O ratio in the rings needs to be elevated above the fiducial value of 0.4 to reproduce the observed intensity in the C_2H, CN, [C I], and NO.

6.5 Conclusions

In this work we have modeled the HD 100546 disk to explore the radial location and intensity of molecular rings seen in HCN, CN, C_2H, NO, and HCO^+ (Booth et al. 2023a). In particular, we investigated under which conditions these molecular rings overlap with those seen in the continuum. The fiducial model provides a good fit to the continuum emission and the emission of CO isotopologues with a deep dust and gas cavity inside 20 au and 15 au respectively, and a deep dust gap and a shallow gas gap from $40 - 175$ au. The abundance of the other molecules of interest, HCN, CN, C_2H, and NO are predicted with a dedicated nitrogen network and that of HCO^+ is predicted with the network presented in Leemker et al. (2021). In summary we find that:

1. The dust and CO isotopologue gas emission in the HD 100546 disk is reproduced by a model with a deep gas ($r < 15$ au) and dust cavity ($r < 20$ au), a deep dust gap and a shallow gas gap with a factor of ten less gas from $40 - 175$ au. A gas gap deeper than one order of magnitude is excluded by the CO isotopologue data.

2. Thermochemical models predict that the molecular rings in HCN, CN, C_2H, NO, and HCO^+ do not follow the dust rings in general, in contrast to the HD 100546 disk observations.

3. Introducing a gas gap in the models increases the UV field, and thus the HCN, CN, C_2H, and NO abundance within the gap. For gas gaps of one to approx. four orders of magnitude deep, the column density of CN, C_2H, and NO increases to above that in the model without a gas gap ($\delta_{\text{gas gap}} = 1$) in certain gap regions. For very deep gas gaps ($\delta_{\text{gas gap}} \sim 10^{-4} - 10^{-5}$) the molecular rings emit at a similar location as the dust rings.

4. An elevated C/O ratio mainly affects the total modelled intensity of [C I], HCN, CN, C_2H, and NO but not the radial location of the emission rings. The modelled CN and C_2H column density and emission increase by roughly one to two orders of magnitude, respectively, when the bulk model C/O ratio is increased from 0.99 to 1.01.

5. A lower background UV radiation field in the models reduces the column density of CN, C_2H, and NO and it increases that of HCN in the outer disk ($r > 100$ au).

6. The flaring index of the disk only has a minor effect on the height of the layer where a high CN abundance is seen, despite models with lower flaring indices being more flat.

7. To reconcile the observed ring locations with those predicted by models, a deep gas gap (factor $\leq 10^{-4}$) is needed to reproduce the double rings seen in CN and C_2H, while the diffuse HCN and HCO^+ emission between the dust rings is best reproduced by a model with $10^{-2} - 10^{-3}$ times less gas.

8. The model predicts ring-shaped NO emission that is not seen in the observations. A lower background UV field by a factor of ten reduces the outer NO ring and creates a double ring seen in C_2H close to the dust rings.

9. The observed intensities of the [C I], CN, and C_2H are only reproduced by the models with an elevated C/O of $\sim 0.8-1.2$. Especially, the C_2H emission requires C/O = 1.00.

This work shows that thermochemical models do not predict molecular rings to be co-spatial with those seen in the dust in general. The constraints from modelling multiple molecules across a gas gap provides a first step towards a full picture of the chemical makeup of the planet-forming material. Multi-line observations of multiple molecules at high spatial and spectral resolution and sensitivity are needed to better constrain the layer from which these molecules emit. These observations can then be used to test thermochemical models and derive the chemical composition of the planet-forming material.

6.6 Acknowledgements

The authors would like to thank Luke Keyte and Dylan T. Natoewal for the useful discussions on the DALI modelling. In addition, Michiel Hogerheijde is thanked for the discussion on water in the HD 100546 disk. This work is supported by grant 618.000.001 from the Dutch Research Council (NWO). Astrochemistry in Leiden is supported by funding from the European Research Council (ERC) under the European Union's Horizon 2020 research and innovation programme (grant agreement No. 101019751 MOLDISK) and by the Netherlands Research School for Astronomy (NOVA).

This paper makes use of the following ALMA projects: 2011.0.00863.S, 2015.1.00806.S, 2016.1.00344.S, 2018.1.00141.S, 2021.1.00738.S. ALMA is a partnership of ESO (representing its member states), NSF (USA) and NINS (Japan), together with NRC (Canada), MOST and ASIAA (Taiwan), and KASI (Republic of Korea), in cooperation with the Republic of Chile. The Joint ALMA Observatory is operated by ESO, AUI/NRAO and NAOJ. The National Radio Astronomy Observatory is a facility of the National Science Foundation operated under cooperative agreement by Associated Universities, Inc.

Table 6.A.1: Continuum wavelengths and molecular transitions.

Molecule	Transition	beam	$n_{\rm crit}$(50 K)	ref.
continuum	0.9 mm (high res.)	$0\farcs05 \times 0\farcs03$ (34°)		1
continuum	0.9 mm (moderate res.)	$0\farcs38 \times 0\farcs30$ (31°)		2
^{12}CO	$J = 2 - 1$	$0\farcs097 \times 0\farcs077$ (−16°)	2.7×10^3	3
^{12}CO	$J = 3 - 2$	$0\farcs35 \times 0\farcs23$ (60°)	9.2×10^3	2
^{12}CO	$J = 7 - 6$	$0\farcs23 \times 0\farcs17$ (30°)	1.2×10^5	4
^{13}CO	$J = 2 - 1$	$0\farcs098 \times 0\farcs077$ (−15°)	2.3×10^3	3
C^{18}O	$J = 2 - 1$	$0\farcs097 \times 0\farcs076$ (−13°)	2.3×10^3	3
C^{17}O	$J = 3 - 2$	$0\farcs39 \times 0\farcs31$ (29°)	8.5×10^3	2
[C I]	$^3P_2 - ^3P_1$	$0\farcs21 \times 0\farcs16$ (28°)	1.4×10^3	5
HCN	$J = 4 - 3$	$0\farcs34 \times 0\farcs23$ (60°)	1.4×10^7	2
CN	$3_{0,7/2,7/2} - 2_{0,5/2,5/2}$	$0\farcs38 \times 0\farcs30$ (29°)	3.8×10^6	2
CN	$3_{0,7/2,9/2} - 2_{0,5/2,7/2}$	$0\farcs38 \times 0\farcs30$ (29°)	3.8×10^6	2
CN	$3_{0,7/2,5/2} - 2_{0,5/2,3/2}$	$0\farcs38 \times 0\farcs30$ (29°)	3.8×10^6	2
$C_2H^{(a)}$	$4_{9/2,5} - 3_{7/2,4}$	$0\farcs37 \times 0\farcs30$ (27°)	1.3×10^6	2
$C_2H^{(a)}$	$4_{9/2,4} - 3_{7/2,3}$	$0\farcs37 \times 0\farcs30$ (27°)	1.2×10^6	2
$NO^{(a)}$	$4_{1,7/2,9/2} - 3_{-1,5/2,7/2}$	$0\farcs47 \times 0\farcs37$ (31°)	2.7×10^4	2
$NO^{(a)}$	$4_{1,7/2,7/2} - 3_{-1,5/2,5/2}$	$0\farcs47 \times 0\farcs37$ (31°)	2.4×10^4	2
$NO^{(a)}$	$4_{1,7/2,5/2} - 3_{-1,5/2,3/2}$	$0\farcs47 \times 0\farcs37$ (31°)	2.4×10^4	2
HCO^+	$J = 4 - 3$	$0\farcs34 \times 0\farcs23$ (60°)	2.6×10^6	2

Notes. $^{(a)}$ All components of a single molecule are added together assuming the emission is optically thin. The critical densities are calculated assuming that the main collision partner is H_2. References: 1. Pineda et al. (2019), 2. Booth et al. (2023a), 3. Pérez et al. (2020) and Wölfer et al. (2023a), 4. Wölfer et al. (2023a), 5. This work.

Appendix

6.A Observed lines

The integrated intensity map and the spectrum of the [C I] emission in the HD 100546 disk is presented in Fig. 6.A.1. An overview of the observations used in this work is presented in Table 6.A.1. In addition to the observations, the critical density for each line is listed as some molecules are found to emit from elevated disk layers below the critical density.

6.B DALI

6.B.1 Model setup

6.B.1.1 Radial and vertical structure

Radially, the gas density follows the solution for a viscously evolving disk model (Lynden-Bell & Pringle 1974; Hartmann et al. 1998; Andrews et al. 2011):

$$\Sigma_{\text{gas full}} = \Sigma_{\text{c}} \left(\frac{r}{r_{\text{c}}} \right)^{-\gamma} e^{-(r/r_{\text{c}})^{2-\gamma}}, \tag{6.4}$$

with $\Sigma_{\text{gas full}}$ the gas surface density of a full disk, Σ_{c}/e the gas surface density at the characteristic radius r_{c}, r the radius, and γ the power law index of the surface density profile. The surface density is defined from the sublimation radius r_{subl} to the outer radius of the disk $r_{\text{out, disk}}$. Assuming a typical dust sublimation temperature of 1500 K, the sublimation radius is located at ~ 0.07 au $\times \sqrt{L/L_{\odot}}$, with L the luminosity of the central star (Dullemond et al. 2001). For the 36 $L_{\odot}$ HD 100546, this corresponds to 0.4 au.

Vertically, we assume that the gas follows a Gaussian distribution with the scale height h given by

$$h = h_{\text{c}} \left(\frac{r}{r_{\text{c}}} \right)^{\psi}, \tag{6.5}$$

with h_{c} the scale height at r_{c} and ψ the flaring index.

The dust in DALI is modeled using a small dust population and a large dust population. Both populations have a minimum grain size of 5 nm but the small grains have a maximum size of 1 μm, whereas the large grains go up to 1 mm. An MRN distribution with an index of -3.5 is used to set the grain sizes a within

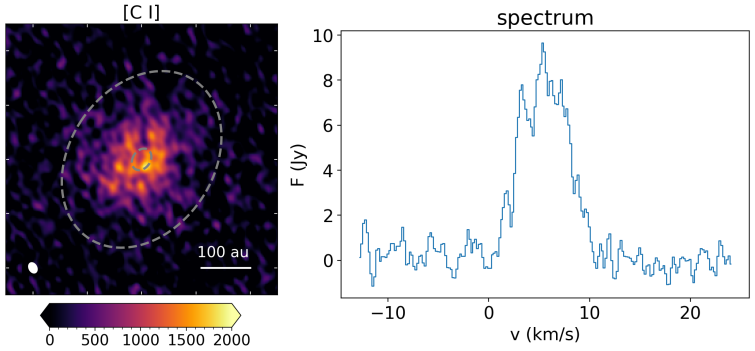

Figure 6.A.1: Observations of [C I] in the HD 100546 disk. Left: integrated intensity map. The grey dashed lines indicate the dust rings in the HD 100546 disk. The beam is indicated in the bottom left corner and a 100 au scale bar is shown in the bottom right corner. Right: spectrum.

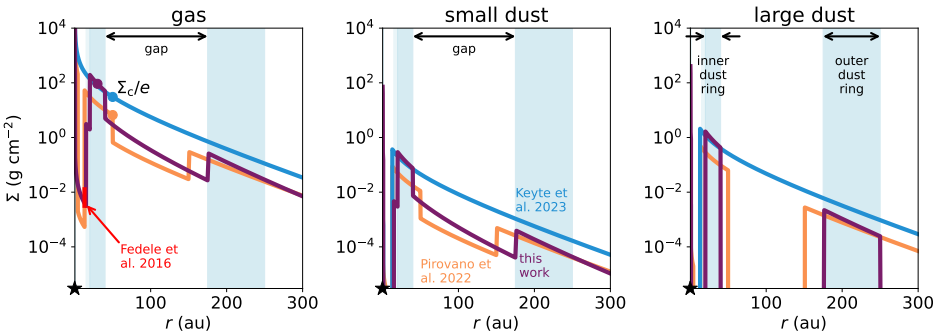

Figure 6.B.1: Surface density of the gas (left), small dust (middle), and large dust (right) in three models for the HD 100546 disk. The blue lines show the full gas disk model presented in Keyte et al. (2023), the orange lines show the model presented in Pirovano et al. (2022), and the purple lines show the model presented in this work. The shaded blue background indicates the dusty inner disk and the dust rings modelled in this work. The surface density Σ_c/e at r_c is indicated with a scatter point in the left panel.

these populations (Mathis et al. 1977). Furthermore, the mass ratio of the large grain population compared to that of the small grains is set by f_{ls} such that the small and large dust in a full disk follow:

$$\Sigma_{\text{s dust full}} = \frac{(1 - f_{ls})\Sigma_{\text{gas full}}}{\Delta_{gd}} \tag{6.6}$$

$$\Sigma_{\text{l dust full}} = \frac{f_{ls}\Sigma_{\text{gas full}}}{\Delta_{gd}}, \tag{6.7}$$

with Δ_{gd} the global gas-to-dust mass ratio. A comparison of the radial structure used in this work to those used by Pirovano et al. (2022) and Keyte et al. (2023) is presented in Fig. 6.B.1.

Edge-on disks show that the large dust is settled to the disk midplane (Villenave et al. 2020). Therefore, the vertical scale height of the large dust is reduced by a settling parameter χ. Thus, the small and large dust are not following the same radial and vertical distributions and the average grain size is calculated per cell, which is used for further calculations.

6.B.1.2 Initial conditions of the chemical networks

The chemical networks are started using mostly molecular initial conditions. Initially, all volatile carbon is locked up in CO and all remaining oxygen is locked up in H_2O such that the C/O ratio is 0.4. In the case of a C/O ratio larger than 1, all oxygen is initialized in the form of CO and the remaining carbon is put in as CH_4. The precise initial partition of nitrogen over N, N_2, and NH_3 in protoplanetary disks is unknown, therefore we rescale the predictions of dark cloud models at 0.3 Myr (N: N_2: NH_3: total number of N atoms = 0.48 : 0.19 : 0.13 : 1;

Walsh et al. 2015). Finally, hydrogen is mainly in H_2 when the model is initialised. An overview of the initial conditions is presented in Table 6.B.1. The chemistry is evolved to the age of the HD 100546 disk of 5 Myr (Arun et al. 2019) and a cosmic ray ionisation rate consistent with that found in other protoplanetary disks of 10^{-18} s^{-1} is adopted (Aikawa et al. 2021).

Table 6.B.1: DALI model parameters

Model parameter	value	Description
Physical structure		
$r_{\rm subl} - r_{\rm dust\ cav\ in}$	$0.4 - 1$ au	dusty inner disk
$\delta_{\rm gas\ cav}, \delta_{\rm s\ dust,\ in}, \delta_{\rm l\ dust,\ in}$	$10^{-5}, 10^{-2}, 10^{-2}$	surface density drop for $r_{\rm subl} < r < r_{\rm cav\ in,\ dust}$
$r_{\rm dust\ cav\ in} - r_{\rm gas\ cav\ out}$	$1 - 15$ au	gas cavity
$\delta_{\rm gas\ cav}, \delta_{\rm s\ dust\ cav}, \delta_{\rm l\ dust\ cav}$	$10^{-5}, 10^{-10}, 10^{-10}$	surface density drop for $r_{\rm dust\ cav\ in} < r < r_{\rm gas\ cav\ out}$
$r_{\rm gas\ cav\ out} - r_{\rm dust\ cav\ out}$	$15 - 20$ au	region outside gas cavity but inside dust cavity
$\delta_{\rm gas\ cav\ edge}, \delta_{\rm s\ dust\ cav\ edge}, \delta_{\rm l\ dust\ cav\ edge}$	$10^{-2}, 10^{-2}, 10^{-10}$	surface density drop for $r_{\rm gas\ cav\ out} < r < r_{\rm dust\ cav\ out}$
$r_{\rm gap\ in} - r_{\rm gap\ out}$	$40 - 175$ au	gap
$\delta_{\rm gas\ gap}, \delta_{\rm s\ dust\ gap}, \delta_{\rm l\ dust\ gap}$	$10^{-1}, 10^{-1}, 10^{-10}$	surface density drop for $r_{\rm gap\ in} < r < r_{\rm gap\ out}$
$r_{\rm l\ dust\ out} - r_{\rm out}$	$250 - 1000$ au	disk region outside the second ring
$\delta_{\rm gas\ out}, \delta_{\rm s\ dust\ out}, \delta_{\rm l\ dust\ out}$	$1, 1, 10^{-10}$	surface density drop for $r_{\rm l\ dust\ out} < r < r_{\rm out}$
$r_{\rm c}$	30 au	Characteristic radius of the surface density profile
$\Sigma_{\rm c}$	250 g cm^{-2}	Sets the gas surface density at the characteristic radius $r_{\rm c}$
$M_{\rm disk}$	5×10^{-2} M$_\odot$	Mass of the disk
γ	1.1	Power law index of the surface density profile
$h_{\rm c}$	0.1	Scale height angle at the characteristic radius $r_{\rm c}$
ψ	0	Flaring index of the disk surface density
PAH abundance	0.1	Gas-phase abundance of PAHs w.r.t. to ISM value
Dust properties		
χ	0.2	Settling of large grains
$f_{\rm ls}$	0.85	Mass-fraction of grains that is large

Table 6.B.1: Continued.

Model parameter	value	Description
$\Delta_{\mathrm{gas/dust}}$	100	Gas-to-dust mass ratio
Stellar properties		
$M_\star$	2.5 $M_\odot$	Mass of the central star
$L_\star$	36 $L_\odot$	Luminosity of the central star
L_{X}	7.9×10^{28} erg s^{-1}	X-ray luminosity of the central star
T_{X}	7×10^7 K	Effective temperature of the X-ray radiation
$\zeta_{\mathrm{c.r.}}$	1×10^{-18} s^{-1}	Cosmic ray ionization rate
Observational geometry		
i	41°	Disk inclination (0° is face-on)
d	108.1 pc	Distance to the star
Chemistry[(1)]		
H	5.2×10^{-5}	
He	1.4×10^{-1}	
N	3.0×10^{-5}	
H_2	5.0×10^{-1}	
H_2O	1.9×10^{-4}	
CO	1.3×10^{-4}	
N_2	1.2×10^{-5}	
NH_3	8.1×10^{-6}	

Table 6.B.1: Continued.

Model parameter	value	Description
Mg^+	1.0×10^{-11}	
Si^+	1.0×10^{-11}	
S^+	1.0×10^{-11}	
Fe^+	1.0×10^{-11}	
$t_{\rm end}$	5 Myr	

Notes. [(1)] Abundance w.r.t. the total number of hydrogen atoms. All molecules start as gas-phase species.

6.B.2 Model predictions

6.B.2.1 Emission profiles and emitting heights of CO isotopologues

The azimuthally averaged radial profiles of the CO isotopologue emission are presented in Fig. 6.B.2. The models with a drop in gas density and small dust density of 1 (no drop) up to 10^{-5} are shown in the same figure with the colored lines. The model without a drop in the gas and small dust density overpredicts the $C^{18}O$ and $C^{17}O$ emission that are the most optically thin and thus the most sensitive to the gas column density. On the other hand, the models with a deeper gap (10^{-2}, 10^{-3}) than the fiducial model (10^{-1}), underpredict the $C^{18}O$ and $C^{17}O$ emission in the gap. Additionally, these models show a clear gap in the brighter ^{12}CO and ^{13}CO lines that is not seen in the observations. This cannot be due to the limited spatial resolution of the observations as the gas gap is fully resolved with 4 beams across the gas gap for $C^{17}O$, the lowest spatial resolution line in this work, and 14 for $C^{18}O$ which has the highest spatial resolution. Outside the gas gap, at the outer dust ring, the $C^{18}O$ emission is overpredicted. However, a lower gas and thus CO isotopologue column density lowers the $C^{17}O$ column density in the gas gap to a value below its minimum value to self-shield. Therefore, a model that fits the $C^{18}O$ in that region will not reproduce the shelf in $C^{17}O$. Therefore, the CO isotopologue observations show that the gas density is depleted by at most a factor of 10^{-1} between the two dust rings under the assumption that the gas and dust gap have the same widths.

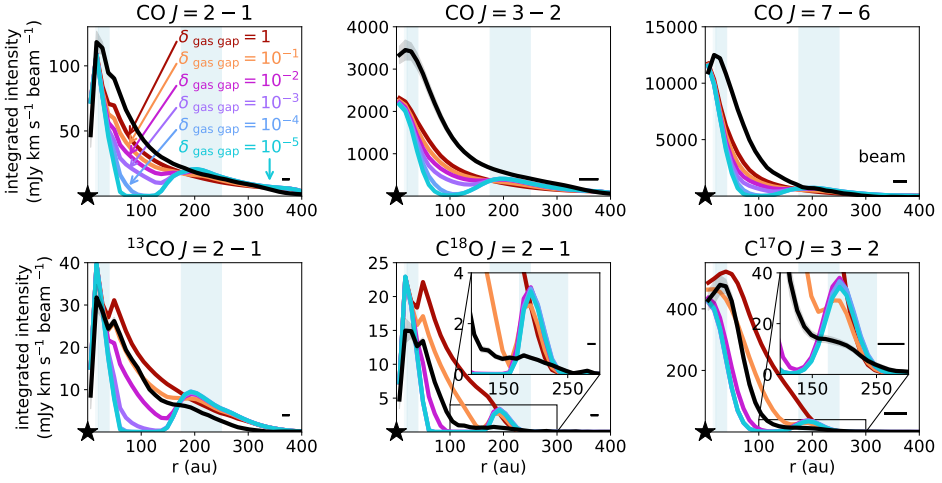

Figure 6.B.2: Azimuthally averaged radial profiles of the dust and CO isotopologue emission observed in the HD 100546 disk (black) together with model predictions for different gaps. In the models, the gas density in the gap ($40 - 175$ au) is reduced by a factor of 1 (no gap; dark red), 10^{-1} (orange), 10^{-2} (pink), 10^{-3} (purple), 10^{-4} (blue), and 10^{-5} (very deep gap; light blue). For all these models, the drop in the small dust density follows that of the gas. The beam is indicated with the horizontal bar in the bottom right corner of each panel.

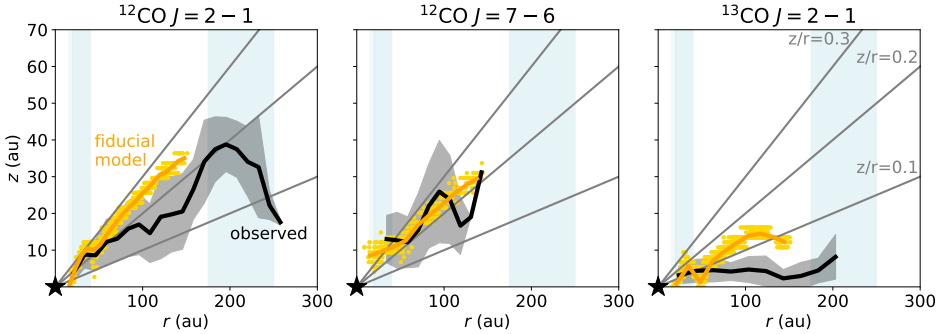

Figure 6.B.3: Emitting heights of the ^{12}CO $J = 2-1$, and $J = 7-6$, and the ^{13}CO $J = 2-1$ transition. The observed emitting heights are presented in black and those of the fiducial model in orange.

The emitting heights of the ^{12}CO $J = 2-1$ and $J = 7-6$ transitions together with that of the ^{13}CO $J = 2-1$ transition are presented in Fig. 6.B.3. These emitting heights are derived using the ALFAHOR package by masking the individual channels after visually inspecting the data (Paneque-Carreño et al. 2023). Wölfer et al. (2023a) found evidence for an asymmetry in the vertical structure between the blue and red shifted sides of this disk. As the DALI models used in this work are azimuthally symmetric, the observed emitting heights are presented as an average of both disk sides.

The fiducial model reproduces the observed emitting height of the ^{12}CO $J = 2-1$ and $J = 7-6$ transitions within 1.5σ for a radius up to 150 au. The lack of vertical segregation between different transitions of one molecule is seen in other DALI models as well (Paneque-Carreño in prep.). Finally, the ^{13}CO emission is seen very close to the disk midplane at a height of only a few au in the observations. The model reproduces the trend that the ^{13}CO emission comes from deeper disk layers than the ^{12}CO, and is consistent within $\sim 2\sigma$ from the observations up to 150 au.

6.B.2.2 Emission profiles and column densities of [C I], HCN, CN, C_2H, NO, and HCO^+ for different gas gaps

The azimuthally averaged radial profiles for the HCN, CN, C_2H, NO, and HCO^+ moment 0 maps presented in Fig. 6.5 are presented in Fig. 6.B.4. Instead of the $C^{18}O$ emission, the profile for the atomic carbon line is presented in the top left corner. The colored lines indicate the models for different gas gap depths between the two dust rings, identical to those in e.g. Fig. 6.B.2. The rings seen in the observations (black) do not coindice with those seen in the models in general. Additionally, the modelled [C I] emission inside 200 au is up to an order of magnitude weaker than what is observed. At larger radii, the model slightly overpredicts the observations, but emission at these scales may be missing due to the small maximum recoverable scale (2" diameter, 108 au radius) of the observation. As the models predict that the molecules are abundant in an elevated layer at

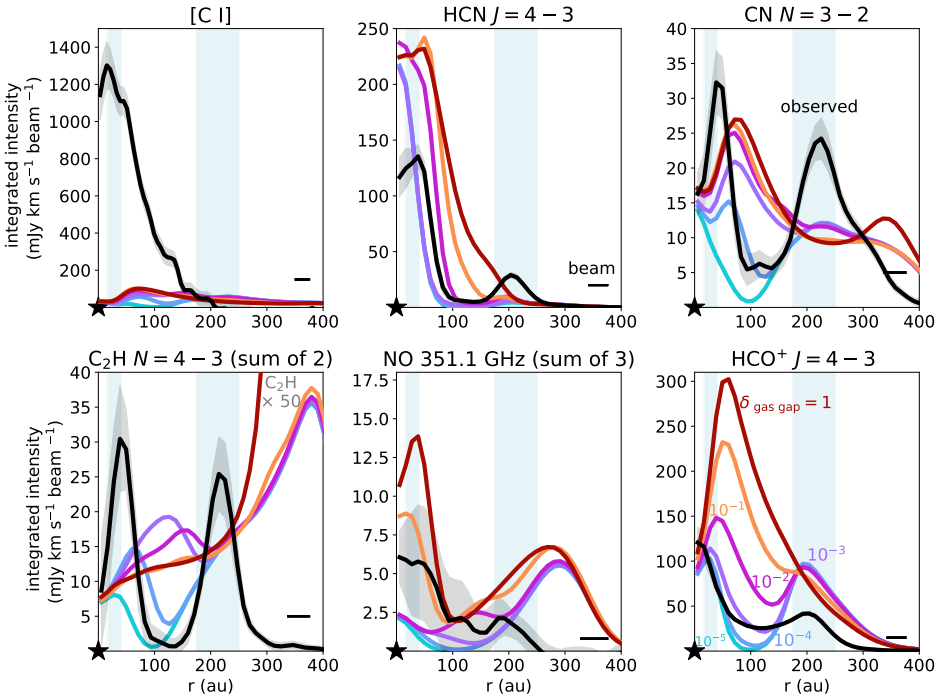

Figure 6.B.4: Azimuthally averaged radial profiles of the [C I], HCN, CN, C_2H, NO, and HCO^+ emission predicted by models with a gas gap depth of 1 (no gap; dark red), 10^{-1} (orange), 10^{-2} (pink), 10^{-3} (purple), 10^{-4} (blue), and 10^{-5} (very deep gap; light blue). The C_2H emission is increased by a factor of 50 for all models to show it on the same scale as the observations. The peak C_2H intensity of the full disk model is 2 mJy km s^{-1} beam^{-1}. The small dust density is dropped by the same factor in the gap. The observed intensities are indicated with the black lines.

$z/r \sim 0.2 - 0.3$, the disk inclination of 41° causes deprojection effects that wash out some of the rings in the CN and move those in C_2H to the location of the outer dust ring. Therefore, the azimuthally averaged radial profiles predicted by a face-on disk model are presented in Fig. 6.B.5.

Similar to the trend seen for the HCO^+ column density, the HCO^+ emission in the gap decreases for deeper gap depths. Even for the shallowest gas gap ($\delta_{\rm gas\ gap} = 10^{-1}$), a shallow gap and a ring are seen in the HCO^+ emission. For deeper gas gaps, the double ring nature of the HCO^+ emission becomes more pronounced (see Fig. 6.B.4 for a more quantitative figure). The modelled intensity in the outer ring lays within a factor of 2.5 of the data for all models. To reproduce the diffuse emission observed in the gas gap, a model with a moderately deep gap of $10^{-2} - 10^{-3}$ is needed. These models as well as those, with even deeper gap of $10^{-4} - 10^{-5}$ match the intensity of the HCO^+ in the gas cavity within 2.5σ, though the models predict a ring at $30 - 40$ au instead of centrally peaked emission.

The CN emission shows a bright inner ring just outside the inner dust ring

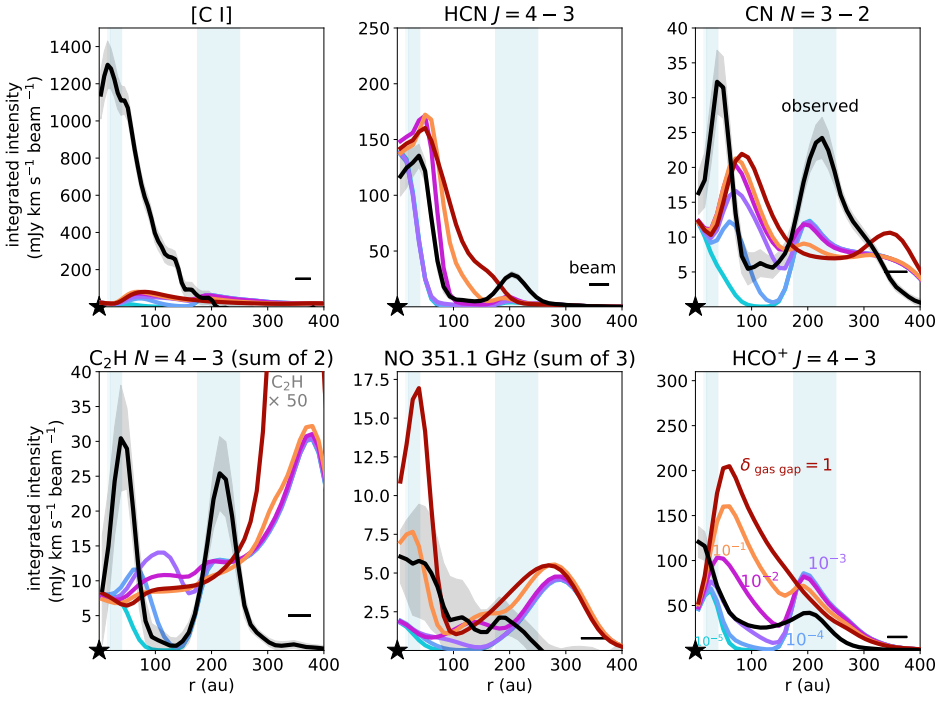

Figure 6.B.5: Same as Fig. 6.B.4 but then for face-on disk. The modelled C_2H emission is increased by a factor of 50 to show it on the same scale as the observations.

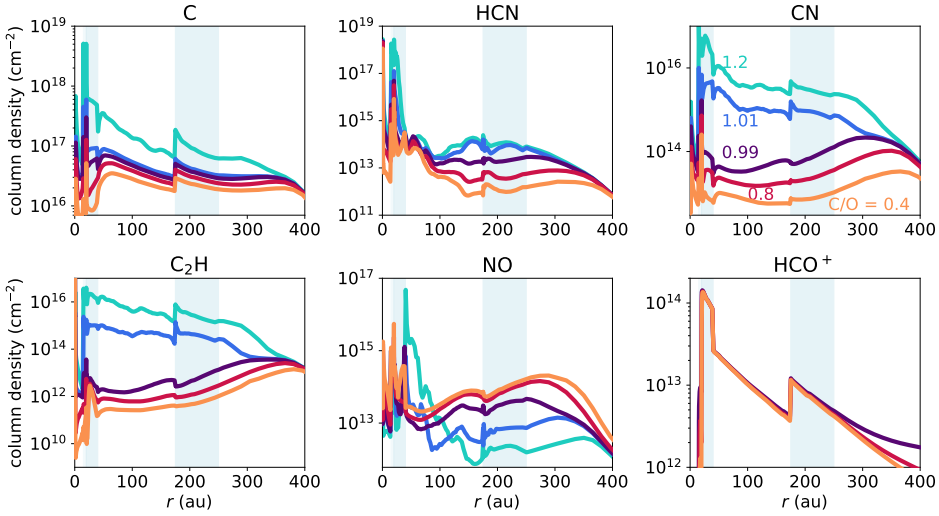

Figure 6.B.6: Column densities of the molecular lines studied in this work for different C/O ratios.

and diffuse emission outwards. For gaps up to $\delta_{\text{gas gap}} = 10^{-3}$, the CN intensity stays more or less constant. For deeper gaps, the CN intensity follows the trends seen in the column density and the inner ring becomes weaker. The models with gaps deeper than 10^{-2} all show emission from an elevated layer as the outer ring consists of two ellipses that are offset along the disk minor axis. This is not seen in the data where the outer CN ring is centred at the position of the star. Apart from this, the model with a deep gap of 4 orders of magnitude less gas resembles the observations quite closely as two distinct rings with an intensity within a factor of ~ 3 of the observations are seen.

C_2H emits as a bright outer ring seen at 375 au due to the high column density in this region. This is much further out than the second ring seen in the data and not affected by the depth of the gas gap. Inside the gap, a ring at low intensity is seen. This ring follows the trend seen in the column density, moves inwards, and brightens as the gas gap becomes deeper. The bright ring seen in the model with a 10^{-4} deep gas gap is only peaks one beam further out than the ring seen in the observations but the modelled intensity is a factor of 40 too low. The inward travelling ring is also seen in the NO emission causing a very bright inner ring for the two models with the deepest gas gaps. The outer ring seen just outside the outer dust ring in the models is not detected in the observations.

Finally, the HCN shows a bright inner ring with an intensity within a factor of two of the observations for the models with a shallow gas gap. For the models with a gap deeper than 10^{-2} a gap and then a very weak ($\lesssim 5$ %) ring at the location of the outer dust ring are seen as highlighted by the white contours in Fig. 6.8. This ring has an intensity of only $3-5$ times weaker than what is observed.

6.B.2.3 Column densities of [C I], HCN, CN, C_2H, NO, and HCO^+ for different C/O ratios

The column densities of C, HCN, CN, C_2H, NO, and HCO^+ for different C/O ratios are presented in Fig. 6.B.6. The column densities of the molecules that contain a carbon atom but no oxygen, C, HCN, CN, and C_2H, all increase with increasing C/O. In particular, the CN and C_2H are sensitive to a C/O ratio increasing from 0.99 to 1.01 as their column densities increase by one and two orders of magnitude, respectively. The NO molecule, that only carries an oxygen atom and no carbon, shows the opposite trend in general. The only exception to this is the high NO column density just outside the inner dust ring in the models with C/O > 1. Finally, the HCO^+ is not sensitive to the C/O ratio in most disk regions as it carries both oxygen and carbon atoms.

6.B.3 Molecular ratios

6.B.3.1 Column density ratios for different gap depths

The HCO^+/CO ratio for gaps up to two orders of magnitude deep is mainly driven by the CO density that is directly proportional to the gas density and the HCO^+ density that goes with the square root of the gas density (see Figs. 6.6 and 6.9). For deeper gaps, CO photodissociation drives the HCO^+/CO ratio up.

Even though no HCO^+ photodissociation is included in the small network, its photodissociation rate is 44 times lower than that of CO (Heays et al. 2017). Therefore, the HCO^+/CO ratio is most sensitive to the gas density.

The C_2H/CO ratio is primarily driven by the drop in the CO column density for gaps up to 10^{-3} as the C_2H column density only starts to drop steeply for gaps deeper than that. This causes the C_2H/CO ratio to saturate at a few 10^{-3} in the outer regions of the 10^{-5} deep gas gap. The CN/HCN ratio rapidly increases when the gap depth is lowered from 10^{-1} to 10^{-2} as the midplane HCN component is removed inside of ~ 80 au. For deeper gaps, the ratio settles between a value of $10 - 100$ inside the gap. Outside the gap, CN is a factor of ten more abundant than HCN.

In contrast to the former ratios, the CN/NO ratio is almost independent of gap depths for a disk with no gas gaps and gaps with up to two orders of magnitude less gas. This is due to the CN and NO column density that are both insensitive to the gap depths for these models. For deeper gaps, both the CN and the NO column density decrease as the gas gap becomes deeper but the CN column density does so at a slower rate than that of NO. Therefore, the CN/NO column density ratio is higher inside the gap than outside.

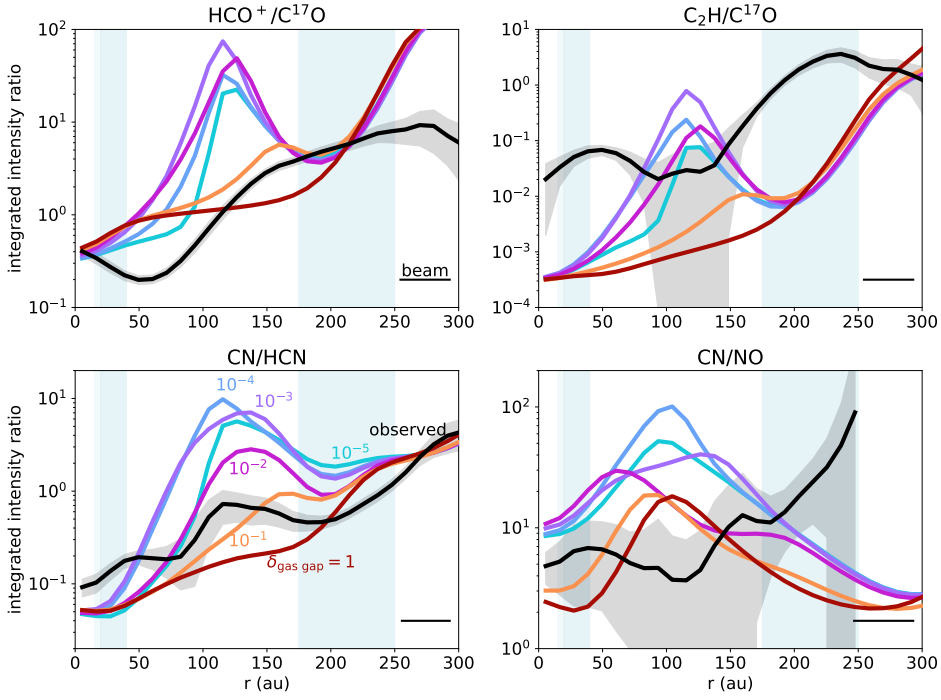

Figure 6.B.7: Emission line ratios of HCO^+/CO (top left), C_2H/CO (top right), CN/HCN (bottom left), and CN/NO (bottom right) for different gas gap depths.

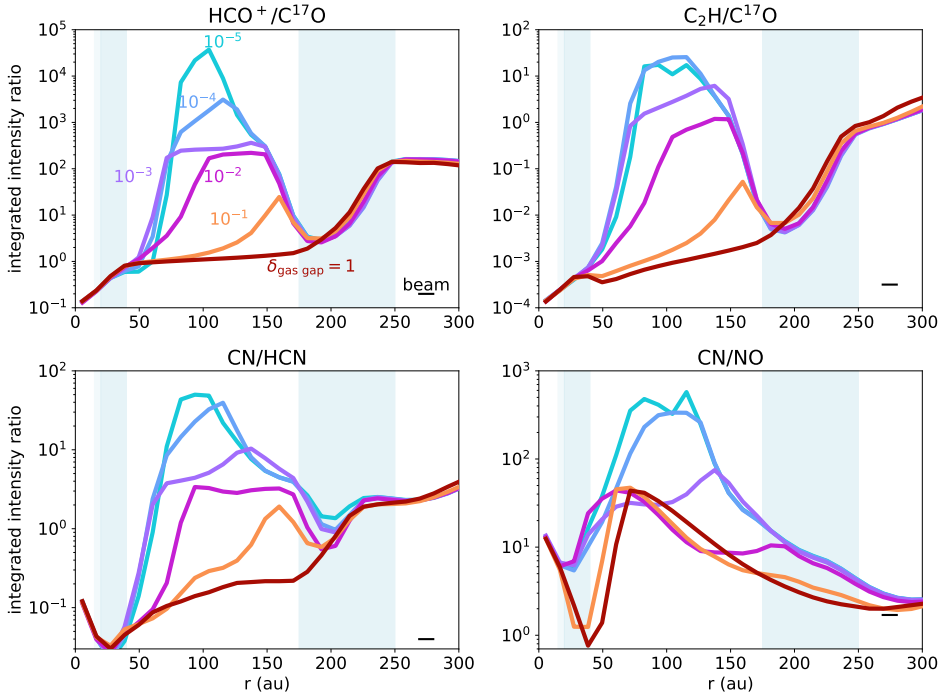

Figure 6.B.8: Same as Fig. 6.B.7 but then for a small beam of 0.″1.

6.B.3.2 Emission line ratios for different gap depths

The corresponding figure for the emission lines is presented in Fig. 6.B.7. For each ratio, the profile of the molecule at the highest spatial resolution is smoothed to the resolution of the image at lower resolution. The modelled ratios of HCO^+/CO, C_2H/CO, CN/HCN, and CN/NO all peak inside the gas gap if the gas gap is at least 10^{-1} deep. The column density ratio increases with gap depth for most regions inside the gas gap, however, the ratio of the integrated intensity does not. This is due to the beam size of the observations. The size and orientation of the beam is such that the dust gap is sampled by only ~ 2 beams across the disk minor axis. Therefore, the line ratio in the gap is dominated by the bright emission at the gap edges. If the models are convolved with a $3-4$ times smaller beam of 0.″1, the gap depth can be traced up to a very deep gas gap of 10^{-4} times less gas, see Fig. 6.B.8.

All models reproduce the $HCO^+/C^{17}O$ ratio seen inside the inner dust ring ($r < 20$ au) and at 200 au where the outer dust ring is located. The observations show that this ratio first decreases in the gap and then increases, whereas the models with a gas gap show a peak at 125 au ($\delta_{\rm gas\ gap} = 10^{-2} - 10^{-5}$) or 150 au ($\delta_{\rm gas\ gap} = 10^{-1}$). The fiducial model with a gap of only one order of magnitude best reproduces the observed ratio outside 100 au. The other models show a ratio of $HCO^+/C^{17}O$ that is too high, indicating that the ionisation is too high or the

abundance of gas-phase water as traced by HCO^+ is too low in the gap. The latter is consistent with the detection of cold, gas-phase water lines originating from $\sim 40 - 300$ au in this disk (van Dishoeck et al. 2021; Pirovano et al. 2022). This is because the modelled HCO^+ abundance does not account for photodesorbed water.

The observed $C_2H/C^{17}O$ ratio peaks just outside the inner dust ring and at the outer edge of the outer dust ring. The models with a gas gap show the opposite behaviour where a peak at ~ 100 au in the $C_2H/C^{17}O$ ratio is predicted. Only the model without a drop in the gas density reproduces the overall trend of the observations with an offset of two orders of magnitude. This offset is driven by the modelled C_2H emission being too weak by that same factor.

The ratio of CN/HCN increases with radius, with a peak seen inside the gas gap and a decrease in the outer dust ring. The models with a gas gap predict the same trend across the disk, with the ratio agreeing within a factor of ~ 4 for the models with gaps up to 10^{-2}. The observations are most consistent with a gap depth of one to two orders of magnitude. The UV field in the models with deeper gas gaps is too intense to reproduce the CN/HCN ratio.

Finally, the CN/NO ratio is presented in the bottom right panel of 6.B.7. The CN/NO ratio of ~ 5 at the inner dust ring is reproduced by the models that do not have a very deep gas gap of $10^{-4} - 10^{-5}$. For the latter models, the NO intensity is much higher, lowering the CN/NO ratio. In the outer dust ring the observed ratio is ~ 10, whereas the models underpredict this by an order of magnitude.

In summary, the line ratios of HCO^+/CO, C_2H/CO, and CN/HCN at the spatial resolution of the observations are only sensitive to the gas gap depths up to a gap with two orders of magnitude less gas. The latter ratio is well reproduced by the models, whereas the $C_2H/C^{17}O$ is not due to the weak C_2H emission. The $HCO^+/C^{17}O$ ratio can be used to trace gas gaps that are up to two orders of magnitude depleted in gas.

6.B.3.3 Column density and line ratios for different C/O ratios

The column density ratios for various molecules as function of the C/O ratio are presented in Fig. 6.B.9. The corresponding emission line ratios are presented in Fig. 6.B.10. The $HCO^+/C^{17}O$ ratio presented in the top left corner does not depend on the C/O ratio of the gas for most disk regions. Only outside the outermost dust ring, the $HCO^+/C^{17}O$ ratio decreases by one order of magnitude down to the observed value for a C/O of 0.99 instead of 0.4.

The $C_2H/C^{17}O$ ratio is driven by the C_2H emission that increases steeply with an increasing C/O ratio. Between the two dust rings, the observed $C_2H/C^{17}O$ is best explained by a model with a C/O just below 1 at 0.99, whereas in the outer dust ring the model with a C/O of 1.01 is close to the observed ratio. The C/O ratio greatly affects the value of the $C_2H/C^{17}O$ ratio, but it does not change the location of the peaks and dips in the profile. Therefore, a global change in the C/O ratio alone cannot explain the observations.

Increasing the C/O ratio increases the CN intensity more than it does so for the HCN. Therefore, the CN/HCN ratio increases with increasing C/O ratio. The

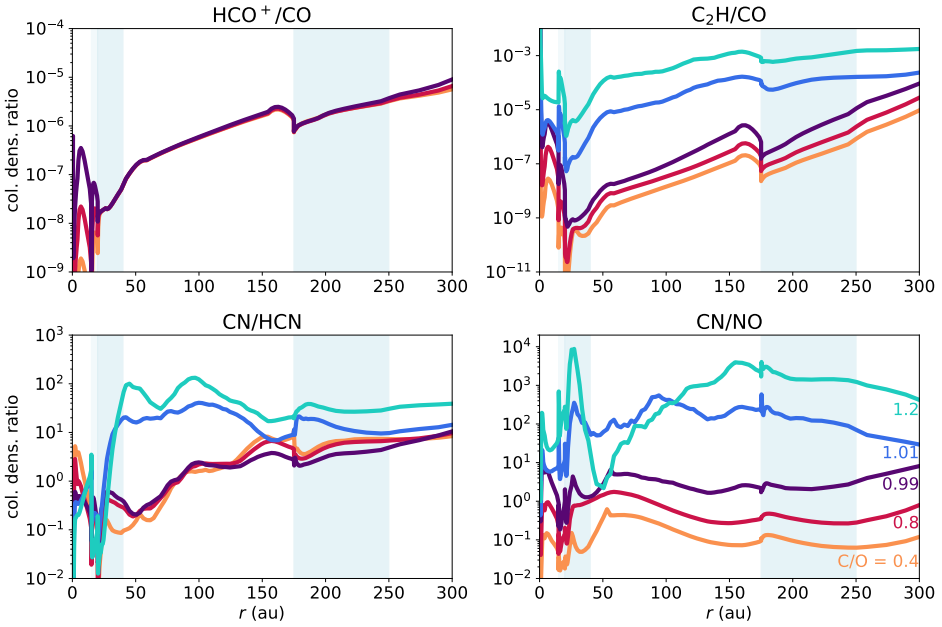

Figure 6.B.9: Column density ratios for different molecules and different C/O ratios.

morphology of the observed ratio is best reproduced by a C/O of 0.4 − 0.8, whereas the value inside the gap is reproduced within $\sim 1\sigma$ for C/O = 0.99. The CN/NO ratio on the other hand is best reproduced by a low C/O of 0.4. In the outer disk, the CN/NO ratio increases by one order of magnitude for a C/O of 0.4, 0.8, 0.99, 1.01, and 1.2. Even though the S/N on the CN/NO ratio is low, the value in the outer dust ring is indicative of a slightly elevated C/O ratio of 0.8.

6.B.4 Background UV

In Fig. 6.B.11, the column densities for models with a lower background UV radiation field are presented. This parameter mainly affects the column densities in the outer disk where a lower UV field lowers the column density of C, CN, C_2H, and NO, whereas it increases that of HCN somewhat due to less efficient photodissociation.

6.B.5 Flaring

The column density and azimuthally averaged radial profiles of CO, HCN, CN, C_2H, NO, and HCO^+ are presented in Fig. 6.B.12 and 6.B.13, respectively. Flaring alone has a minor to no effect on the CO and HCO^+ column densities, whereas those of HCN, CN, C_2H, and NO do generally increase with decreasing flaring indices. These differences in the column densities are partially countered by the changing temperature structure as less flared disks intercept less UV.

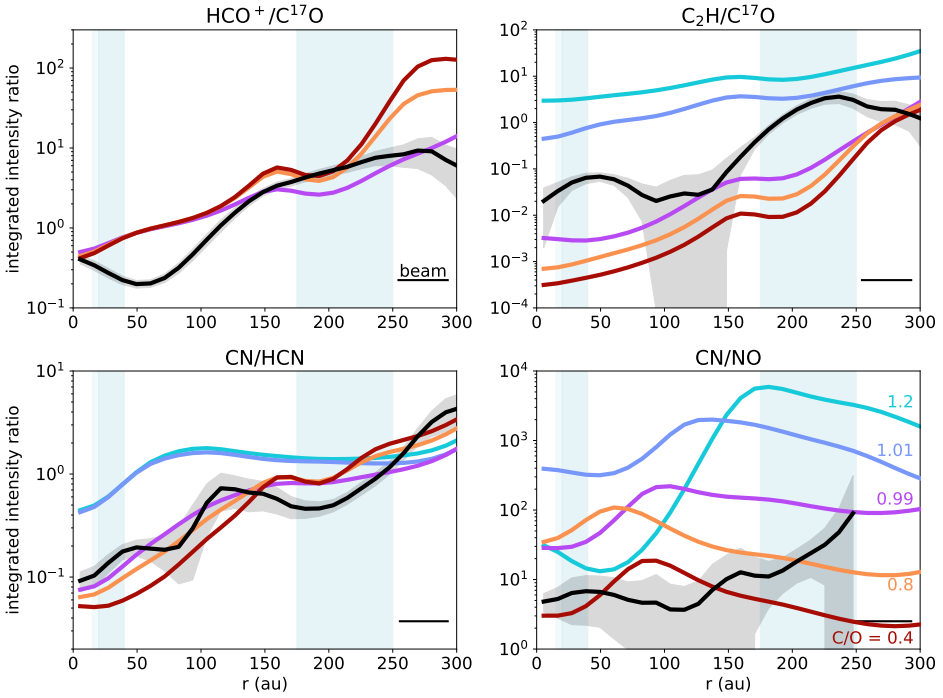

Figure 6.B.10: Emission line ratios of HCO^+/CO (top left), C_2H/CO (top right), CN/HCN (bottom left), and CN/NO (bottom right) for different gas gap depths. The black line indicated the observed emission line ratio for each pair.

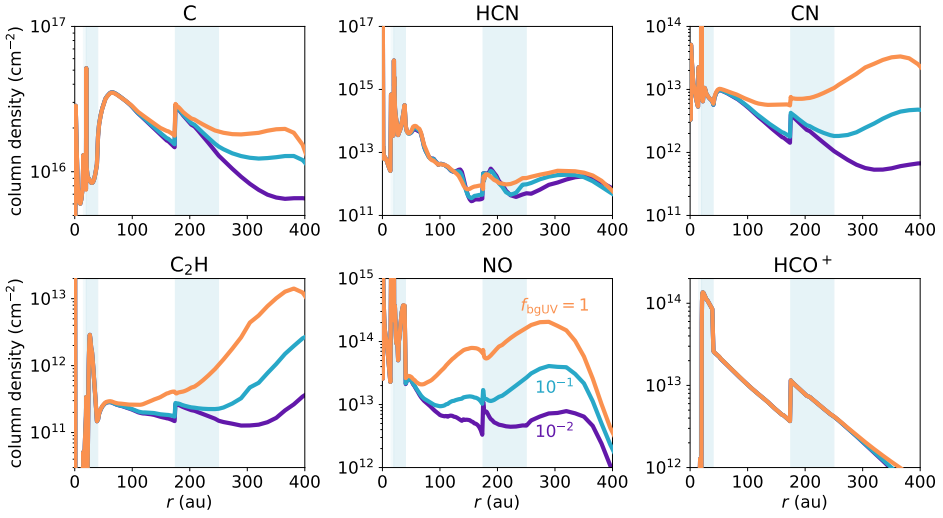

Figure 6.B.11: Column densities of different molecules studied in this work for different background UV radiation fields.

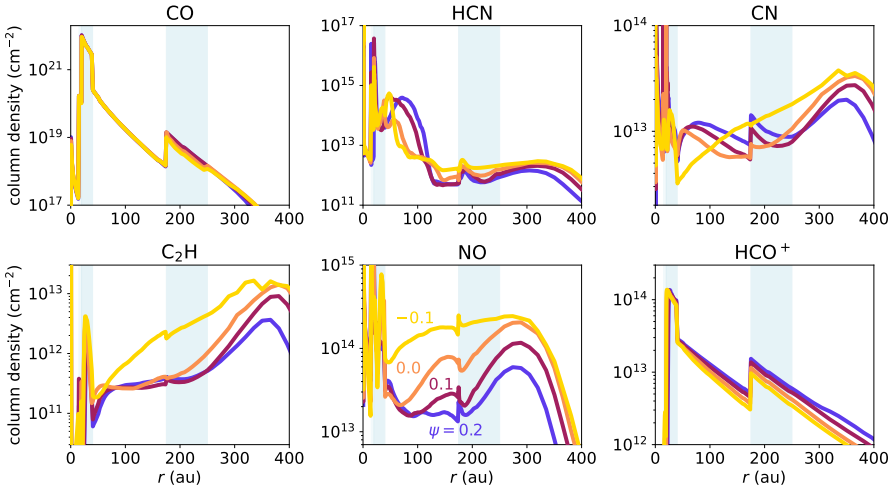

Figure 6.B.12: Column densities of different molecules studied in this work for different flaring indices.

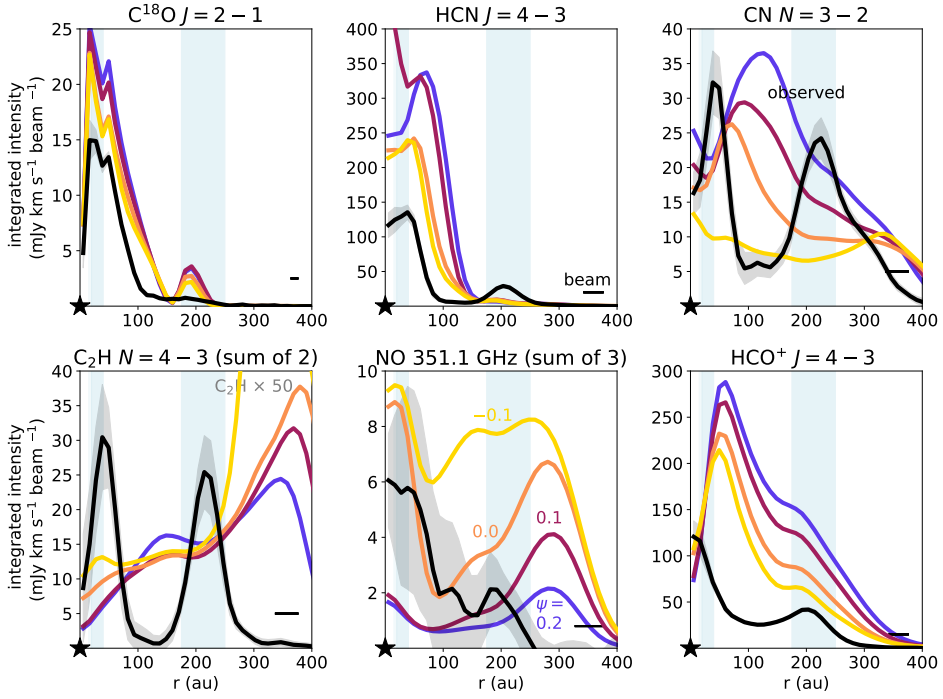

Figure 6.B.13: Molecular line emission of different molecules studied in this work for different flaring indices.